Bioactive Materials 27 (2023) 560–573

Contents lists available at ScienceDirect

Bioactive Materials

journal homepage: www.keaipublishing.com/en/journals/bioactive-materials

# Tellurium-driven maple leaf-shaped manganese nanotherapeutics reshape tumor microenvironment via chemical transition *in situ* to achieve highly efficient radioimmunotherapy of triple negative breast cancer

Wei Huang [a], Sujiang Shi [d], Haoran Lv [a,b], Zhenyu Ju [c], Qinghua Liu [a,b,**], Tianfeng Chen [a,d,*]

[a] Jieyang Medical Research Center, Jieyang People's Hospital, Tianfu Road 107, Rongcheng District, Jieyang, Guangdong, 522000, China
[b] Department of Nephrology, The First Affiliated Hospital, NHC Key Laboratory of Clinical Nephrology (Sun Yat-Sen University) and Guangdong Provincial Key Laboratory of Nephrology, Sun Yat-sen University, Guangzhou, China
[c] Key Laboratory of Regenerative Medicine of Ministry of Education, Institute of Aging and Regenerative Medicine, Jinan University, Guangzhou, 510632, China
[d] Department of Chemistry, Jinan University, Guangzhou, 510632, China

ARTICLE INFO

*Keywords:*
Radioimmunotherapy
Triple negative breast cancer
Tellurium
Manganese carbonate
Tumor microenvironment

ABSTRACT

The therapeutic efficacy of radioimmunotherapy against triple negative breast cancer (TNBC) is largely limited by the complicated tumor microenvironment (TME) and its immunosuppressive state. Thus developing a strategy to reshape TME is expected to achieve highly efficient radioimmunotherapy. Therefore, we designed and synthesized a tellurium (Te)-driven maple leaf manganese carbonate nanotherapeutics ($MnCO_3$@Te) by gas diffusion method, but also provided a chemical catalytic strategy *in situ* to augment ROS level and activate immune cells for improving cancer radioimmunotherapy. As expected, with the help of $H_2O_2$ in TEM, $MnCO_3$@Te heterostructure with reversible $Mn^{3+}/Mn^{2+}$ transition could catalyze the intracellular ROS overproduction to amplify radiotherapy. In addition, by virtue of the ability to scavenge $H^+$ in TME by carbonate group, $MnCO_3$@Te directly promote the maturation of dendritic cells and macrophage M1 repolarization by stimulator of interferon genes (STING) pathway activation, resulting in remodeling immuno-microenvironment. As a result, $MnCO_3$@Te synergized with radiotherapy and immune checkpoint blockade therapy effectively inhibited the breast cancer growth and lung metastasis *in vivo*. Collectively, these findings indicate that $MnCO_3$@Te as an agonist, successfully overcome radioresistance and awaken immune systems, showing promising potential for solid tumor radioimmunotherapy.

## 1. Introduction

Due to the risk factors related to modern lifestyles, the incidence rate of cancer has increased rapidly worldwide [1]. Breast cancer is the cancer with the highest incidence rate among women [2]. And then triple negative breast cancer (TNBC), which accounts for 10–20% of breast cancers relative to other breast cancers, lacks estrogen, progesterone, and human epidermal growth factor receptor 2 (HER-2), leading to its highly malignant, aggressive nature and tendency to relapse after chemotherapy [3]. Therefore, there is still no effective and specific therapy in clinical practice, which encourages scientists to discover and develop novel therapies for TNBC targeted therapy.

In recent years, cancer immunotherapy aims to remodel the patient's own immune system and realize the recognition and destruction of cancer cells, has made a major breakthrough in the field of oncology, especially immune checkpoint blockade therapy (ICB) [4,5]. Although the application of CTLA-4 and anti-PD-1 therapy have produced impressive clinical effects, the effectiveness of these methods still depends on the presence of tumor inflammation and the activation of the patient's immune system [6,7]. Unfortunately, TNBC is considered to be a typical immune "cold" tumor, in which the suppressed tumor microenvironment (TME) makes it impossible for cytotoxic T cells to be

*Abbreviations:* TNBC, Triple negative breast cancer; Te, Tellurium; TME, Tumor microenvironment; STING, Stimulator of interferon genes; MnCO3, Manganese carbonate; CTLs, Cytotoxic T lymphocytes; ROS, Reactive oxygen species.

Peer review under responsibility of KeAi Communications Co., Ltd.

* Corresponding author. Jieyang Medical Research Center, Jieyang People's Hospital, Tianfu Road 107, Rongcheng District, Jieyang, Guangdong, 522000, China.
** Corresponding author. Jieyang Medical Research Center, Jieyang People's Hospital, Tianfu Road 107, Rongcheng District, Jieyang, Guangdong, 522000, China.
*E-mail addresses:* liuqhua6@mail.sysu.edu.cn (Q. Liu), tchentf@jnu.edu.cn (T. Chen).

https://doi.org/10.1016/j.bioactmat.2023.04.010
Received 26 February 2023; Received in revised form 9 April 2023; Accepted 11 April 2023

effectively activated, thus unable to trigger a strong anti-tumor immune response [8,9]. So it is of great significance to develop an strategies to reshape TME from "cold tumor" to "hot tumor, so as to restore the anti-tumor T cell response [10,11].

Meanwhile, radiotherapy is currently the mainstream clinical strategy for 70% of cancer patients including TNBC patients, that is utilize high intensity ionizing radiation to induce DNA damage or generate reactive oxygen species (ROS) to induce tumor inhibition [12–15]. However, radiation resistance and toxic side effects are the important culprit in reducing efficiency of radiotherapy [16–18]. Of note, recent studies indicated that the combination strategy of RT and ICB provides an opportunity to augment immune responses against tumors [19,20]. Sun et al. designed a stabilized theranostic NIR-II nanoprobe (QD-Cat-RGD) and found that under the action of QD-Cat-RGD probe, the synergistic effect of radiotherapy and immunotherapy can improve the inhibition of immunogenic radiotherapy and inhibit cancer metastasis [21]. Impressively, this combination strategy has also been implemented in many clinical trials and was exhibits superior therapeutic effects [22–24]. Unfortunately, even under this strategy, the stimulation efficiency of cytotoxic T cells still limited by suppressive tumor immune microenvironment (TIME) that is caused by the acidity of tumor [25–28]. Specifically, the acidity in tumor tissue can lead to the immune tolerance of cytotoxic T lymphocytes (CTLs) and induce the massive infiltration of immunosuppressive cells including myeloid-derived suppressor cells (MDSCs) and regulatory T cells (Tregs) etc [29–31]. Therefore, relieving acidic microenvironment of tumor plays an important role in enhancing tumor immune response by recovering of functions of antitumor T cells [32].

Nowadays, with the rapid development of nanotechnology, scientists have developed many nanosystems to enhance radiosensitivity of tumor cells or achieve antiacid therapy for tumors [33]. Tellurium (Te) belongs to the oxygen group, which was found to be similar to the element selenium (Se), has antioxidant and antitumor properties [34–36]. For example, Wu et al. found Te nanowires (TeNWs) triggered by hydrogen peroxide ($H_2O_2$) in TME to produce toxic $TeO_6^{6-}$ that could be used as prodrug for highly selective cancer chemotherapy [37]. Moreover, Te semiconductor including Te nanorods (TeNDs), nanostars, nanosheets and nanodots have been successively applied in photothermal therapy, photodynamic therapy, radiotherapy and immunotherapy [38–40]. Nevertheless, these Te-based nanosystems remain plagued by short blood circulation time, weak biocompatibility and rapid clearance by reticuloendothelial system (RES).

Manganese carbonate ($MnCO_3$) semiconductor is widely used in ultrasound/magnetic resonance imaging (MRI)-mediated tumor ultrasound therapy/photodynamic therapy due to its widely bandgap, excellent biocompatibility and pH responsiveness etc [41–43]. More excitingly, it is recently showed that Mn element is an innate immune activation adjuvant by activating stimulator of interferon genes (STING) pathway [44,45]. Besides, it is worth noting that like calcium carbonate and calcium phosphate, $MnCO_3$ nanosystem may possess unique advantages in neutralizing tumor acidity in theory [46–48]. However, the complex synthesis method and the large size after synthesis greatly limit its wide application in the field of biomedicine.

Therefore, considering the above research background, we not only introduce a gas diffusion method to synthesize a Te-driven maple leaf-shaped manganese carbonate nanotherapeutics ($MnCO_3$@Te), but also provide a catalytic strategy *in situ* to remodel the TME and enhance ROS overproduction for achieving simultaneous radioimmunotherapy. As illustrated in Scheme 1, the nanosystem has several important features: (i) the reasonable design of $MnCO_3$-coated Te has greatly changed the diameter and morphology of $MnCO_3$ crystal and realized the controllable transformation of morphology. (ii) in the TME, $MnCO_3$@Te realized the burst release of $Mn^{2+}$ and then triggered the intracellular ROS generation by Fenton-like reaction, thereby realizing precision radiotherapy with invisible side-effects. (iii) $MnCO_3$@Te scavenged $H^+$ in the TME, allowing the maturation of dendritic cells and macrophage M1 repolarization by STING pathway activation, thereby relieving suppressive TIME. (iv) with the assistance of the anti-PD-L1 checkpoint blockade, $MnCO_3$@Te synergized with radiotherapy effectively inhibited the breast cancer growth and lung metastasis *in vivo*. Collectively, this study provides a valid tactic for facile synthesis of shape-controllable $MnCO_3$ nanosystems for solid tumor radioimmunotherapy.

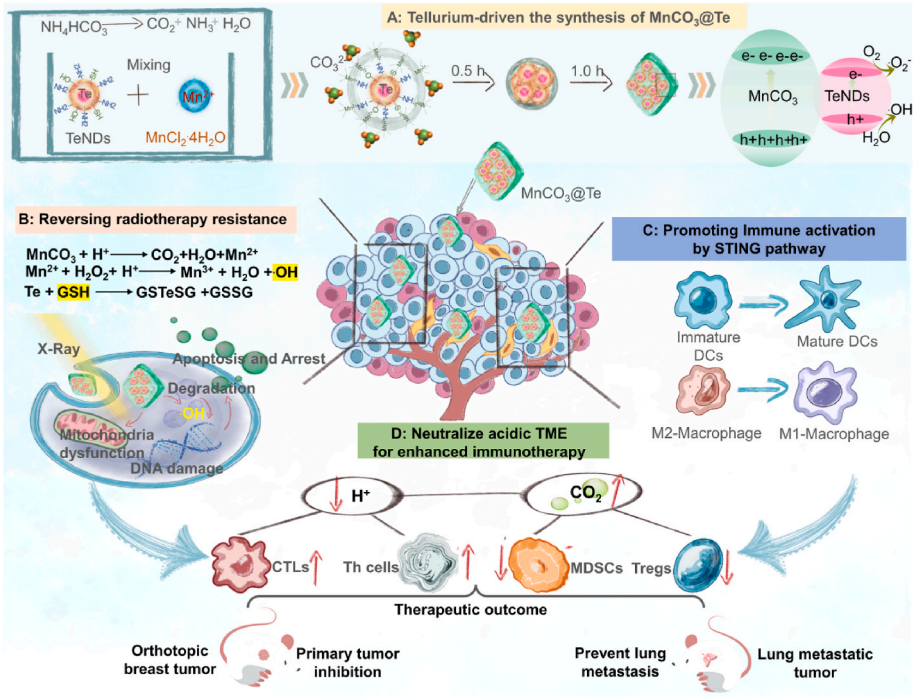


**Scheme 1.** Schematic illustration of Te-driven $MnCO_3$ nanotherapeutics synthetic procedure and its mechanism for anticancer and antimetastasis activity in radioimmunotherapy via reshaping tumor microenvironment.

## 2. Result and discussion

### 2.1. Design, synthesis, and characterization of $MnCO_3$@Te nanotherapeutics

Here as illustrated in Scheme 1, we provide a simple one-pot strategy for the synthesis of maple leaf-shaped Te-loading manganese carbonate nanotherapeutics that can be serve as radiosensitizers and immunotherapeutic boosters to simultaneous enhance radioimmunotherapy by remodeling TME. Firstly, TeNDs with bovine serum albumin (BSA) surface decoration were synthesized as previously described [38]. Transmission electronic microscope (TEM) images in Fig. S1 showed the size of TeNDs was between 10 and 30 nm. Then, the acquired TeNDs was added to $MnCl_2$ solution for mixed for 30 min. Next, the mixture was put into enclosed chamber containing $NH_4HCO_3$ solution for 1.5 h to obtain $MnCO_3$@Te composite nanosystem. As shown in Fig. 1a–d, unlike bare $MnCO_3$ nanosystem synthesized in ethanol phase, which exhibited a tridimensional rhomboid morphology with an average diameter of about 600 nm, the obtained $MnCO_3$@Te in the aqueous phase presented a shape similar to a maple leaf, with a diameter of about 220 nm under observation by TEM and scanning electron microscopy (SEM). As analyzed by elemental mapping and EDX (Fig. 1e and Fig. S2), Mn, Te, N, C and O elements were found to be homogeneously distributed in the $MnCO_3$@Te nanosystems, demonstrating TeNDs were successfully wrapped in $MnCO_3$ nanosystems.

To demonstrate the key role of TeNDs on the synthesis of $MnCO_3$, we allowed the growth of TeNDs within $MnCO_3$ for various reaction times, followed by TEM imaging. As shown in Fig. 1f, after 0.5 h of reaction, most of the products appear in the form of nanospheres and TeNDs could be clearly observed in the middle. 1 h later, the edge of the ball grew a

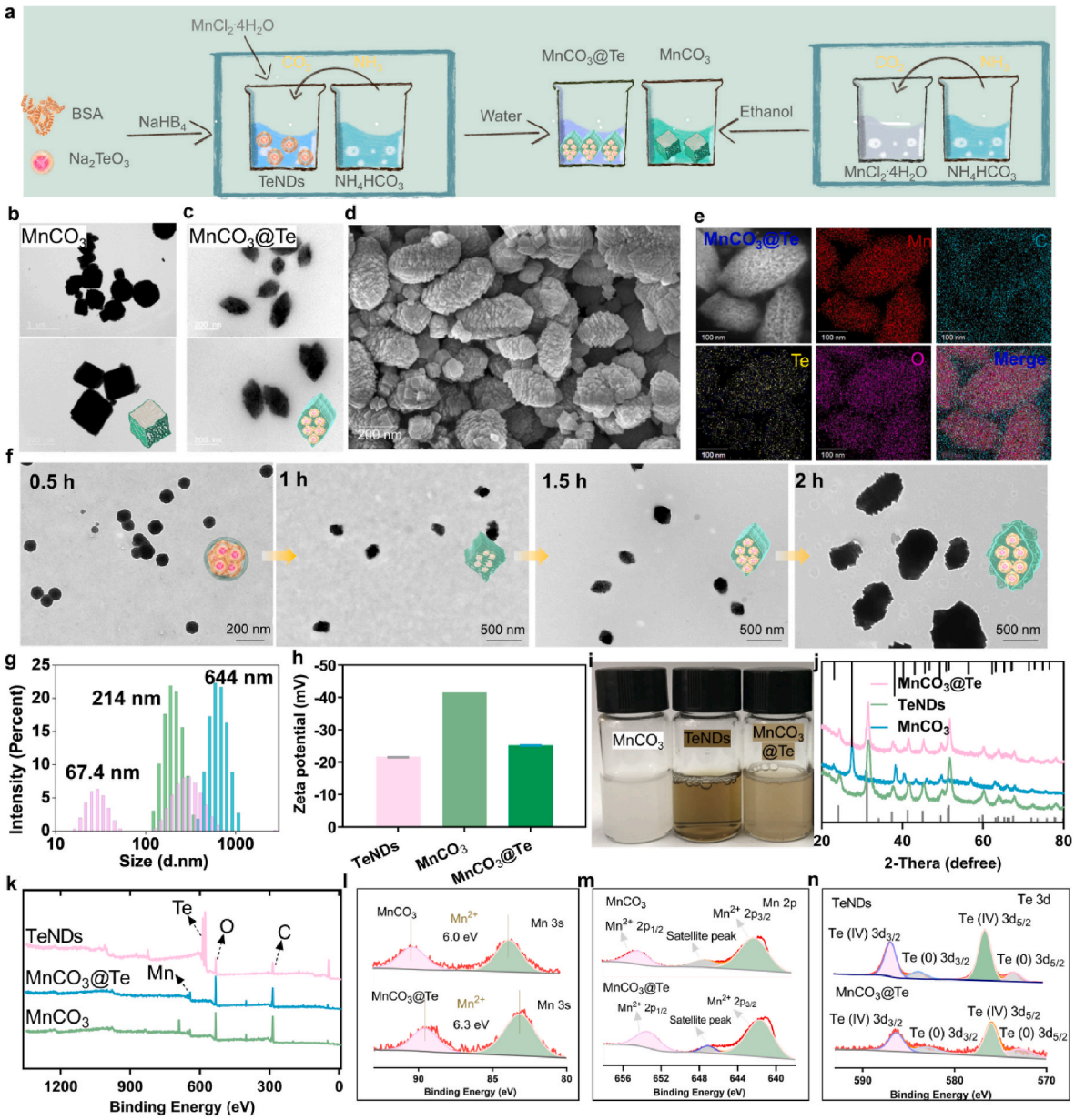


**Fig. 1. Schematic, synthesis and characterization of $MnCO_3$@Te.** (a) Synthetic scheme including TeNDs, $MnCO_3$ and $MnCO_3$@Te. TEM images of $MnCO_3$ (b) and $MnCO_3$@Te (c) nanosystems under different scales. (d) SEM image of $MnCO_3$@Te. (e) Elemental mapping analysis of $MnCO_3$@Te. (f) TEM images of $MnCO_3$@Te obtained at different reaction times to show the reaction progress. (g–h) Hydrodynamic diameters and zeta potentials of $MnCO_3$, TeNDs and $MnCO_3$@Te. (i) Digital photograph of $MnCO_3$, TeNDs and $MnCO_3$@Te in water solution. (j) XRD analysis of $MnCO_3$, TeNDs and $MnCO_3$@Te. (k) Whole XPS spectrum of $MnCO_3$, TeNDs and $MnCO_3$@Te. (l–n) High-resolution XPS spectrum of Mn3s, Mn 2p and Te3d in $MnCO_3$ and $MnCO_3$@Te nanomaterials.

"rhombus", similar to a tridimensional rhomboid. At 1.5 h, the morphology evolved into maple leaf in shape, and finally at 2 h, the crystal continued to grow longitudinally to form "nanorod". Meanwhile, we investigated the influence of BSA on the morphology of $MnCO_3$ by using BSA to replace TeNDs. From Fig. S3, we observed similar phenomenon to $MnCO_3$@Te reaction for 2 h, but the size of $MnCO_3$@BSA was more than 1000 nm. As previous studies showed, BSA can participate in the synthesis of nanomaterials to achieve the goal of modifying and stabilizing nanoparticles [49]. Therefore, based on these results we acquired, we conclude that BSA modified on the surface of TeNDs has key influence on the morphology and diameter of $MnCO_3$@Te nanosystems. This may be due to the preferential coordination between the chemical groups on the BSA and $Mn^{2+}$, which affects the crystal formation. Moreover, dynamic light scattering (DLS) results revealed the average hydrodynamic sizes of TeNDs, $MnCO_3$ and $MnCO_3$@Te were about 67.4, 644 and 214 nm, respectively and the corresponding

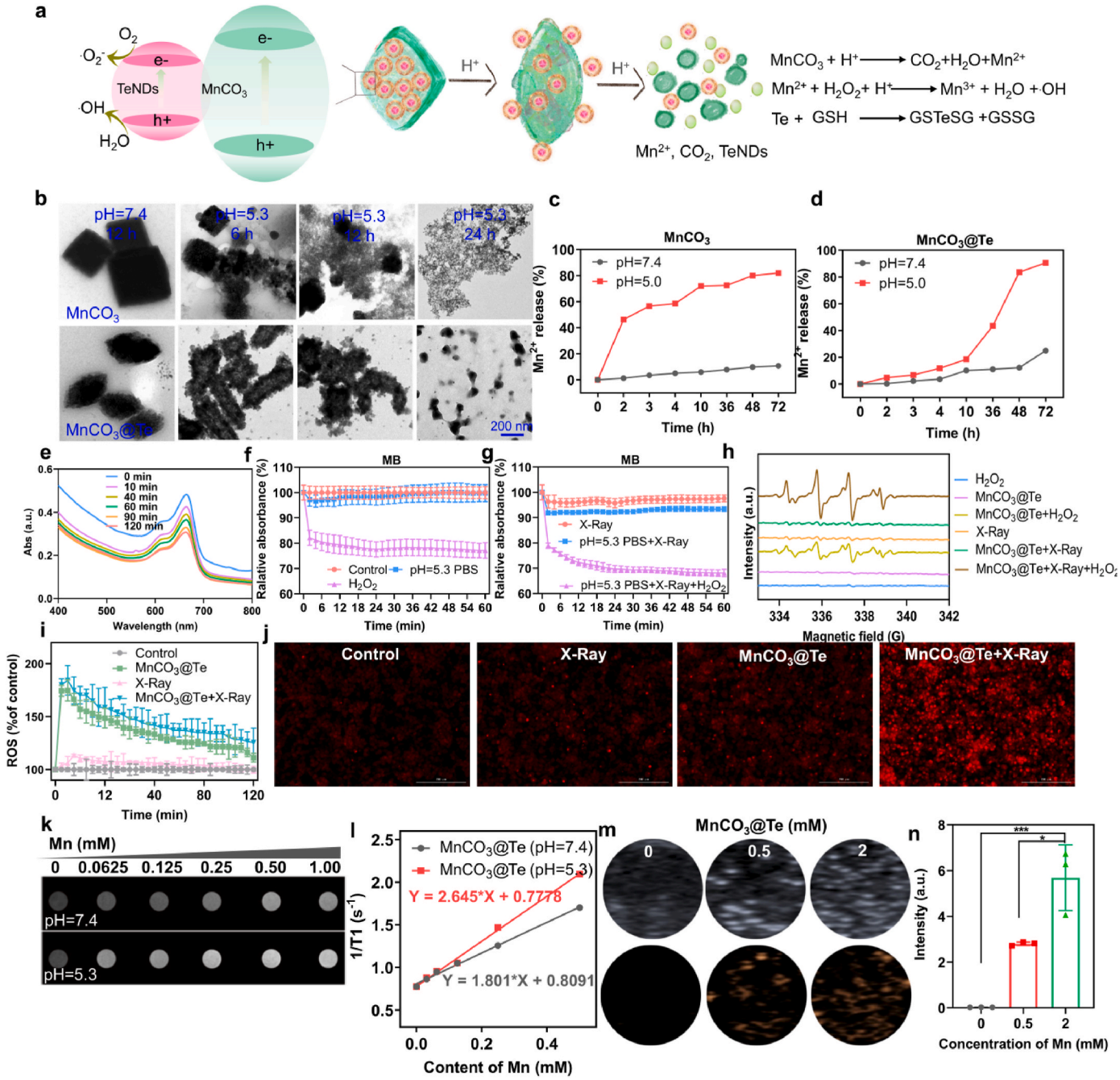


**Fig. 2. Responsive behaviors of $MnCO_3$@Te improve ROS generation through fenton-like reaction and realizes efficient MR imaging and ultrasonic imaging *in vitro*.** (a) Schematic illustration reflecting the $MnCO_3$@Te heteronanostructures and its bioresponsibility in TME. (b) TEM image of $MnCO_3$ and $MnCO_3$@Te after incubation in PBS solution with different pH values for different times. (c–d) Release behaviors of $Mn^{2+}$ from $MnCO_3$@Te in pH 7.4 and 5.0 environment within 72 h. (e) The absorbance spectra of MB solutions containing $MnCO_3$@Te at different time periods under X-Ray radiation for detection of •OH. (f–g) With/without X-Ray irradiation, the degradation curves of MB probes at 655 nm after incubation under various treatments. (h) ESR spectra of detection of •OH of $MnCO_3$@Te immersed in $H_2O_2$ solution under X-Ray irradiation. (i) Intracellular ROS levels in MDA-MB-M231 cells, determined by DHE probe. (j) Representative fluorescence images of ROS level in MDA-MB-M231 cells after different treatments. T1-weighted MR imaging (k) and T1 relaxation rates (l) of $MnCO_3$@Te with different concentrations after incubation with different conditions. (m–n) Ultrasound imaging and statistical data of $MnCO_3$@Te in acid buffer.

zeta-potentials were −21.6, −41.5 and −25.3 mV, respectively (Fig. 1g and h). This phenomenon was due to changes in reactive solvents affecting the particle size of $MnCO_3$ nanomaterials. On the other hand, in order to prove the universality of this synthesis strategy, we attempted to prepare $CaCO_3$@Te nanosystem by using the same preparation method as $MnCO_3$@Te nanosystem. As shown in Fig. S4, TeNDs were highly homogeneous and monodispersed in $CaCO_3$ nanomaterials, which revealed the method was suitable for the synthesis of various carbonate nanomaterials.

Moreover, we could observe that after loading TeNDs, the color of $MnCO_3$@Te solution changes from milky white to light brown (Fig. 1i). Besides, according to the powder X-ray diffraction (XRD) pattern analysis, the diffraction peak of $MnCO_3$@Te was well matched with that of bare $MnCO_3$ and TeNDs (Fig. 1j). Furthermore, the X-ray photoelectron spectroscopy (XPS) was introduced to analysis the chemical composition and valence. As shown in Fig. 1k, characteristic peaks of Te 3d, Mn2p, C1s and O1s were clearly observed. Then, the high-resolution spectra of Mn3s, Mn2p and Te3d were further analyzed as presented in Fig. 1l-n. In general, the valence state of manganese in nanosystem can be determined by the multiple splitting of Mn3s [50]. The separation of peak energies (ΔE) in $MnCO_3$ and $MnCO_3$@Te Mn 3s spectra were 6.0 eV and 6.3 eV, which indicated that the valences of Mn in $MnCO_3$ and $MnCO_3$@Te nanosystems mainly belong to $Mn^{2+}$. Besides, the peaks at 641.7, 647.2, and 653.5 eV were attributed to $Mn^{2+}$ $2p_{3/2}$, satellite peak, and $Mn^{2+}$ $2p_{1/2}$, respectively. Moreover, Te 3d peaks could be subdivided into four peaks located at 572.9, 576.0, 583 and 586.2 eV, which attributed to $Te^0$ $3d_{5/2}$, $Te^{n+}$ $3d_{5/2}$, $Te^0$ $3d_{3/2}$ and $Te^{n+}$ $3d_{3/2}$. Overall, these experiments commonly indicate that the $MnCO_3$@Te formulation with changeable morphology was conducted successfully.

### 2.2. Response performance of $MnCO_3$@Te in TME

It is known that $MnCO_3$ is stable at neutral and alkaline pH environment, but it can be decomposed into $Mn^{2+}$ and $CO_2$ gas in acid buffer (s 2a) [51]. Therefore, we recorded the morphology changes and the release of $Mn^{2+}$ after incubation of $MnCO_3$ and $MnCO_3$@Te in PBS with different pH values (7.4 and 5.3) in different treatment time via TEM and inductively coupled plasma mass spectrometry (ICP-MS). As shown in Fig. 2b–d, although the morphology of $MnCO_3$ and $MnCO_3$@Te exhibited no obvious change in pH 7.4 solution, we found $MnCO_3$ and $MnCO_3$@Te could rapidly be degraded by time-dependent manner. Meanwhile, quantitative analysis also proved that weak acidic environment promoted the release of $Mn^{2+}$ rapidly. The results suggested that the $MnCO_3$@Te is excellent acidity-responsive nanocarriers.

Previous studies have shown that the $Mn^{2+}/Fe^{3+}$ would be promote genernation of highly cytotoxic hydroxyl radical (•OH) by triggering Fenton/Fenton-like reactions in tumor cells [52,53]. Hence, to investigate the effect of $MnCO_3$@Te on generate •OH, we used methylene blue (MB) to examine the generation of •OH [54]. Meanwhile, to simulate the actual catalytic situation in tumor cells, $MnCO_3$@Te was incubated in pH 5.3 PBS solution containing 10 mM $H_2O_2$. As shown in Fig. 2e, from the absorption spectra of MB, under X-Ray irradiation, the characteristic absorption peak gradually decreased with time in the presence of $H_2O_2$ at pH 5.5, indicating •OH production. It was worth noting that without X-Ray irradiation, $MnCO_3$@Te + $H_2O_2$ generated the signal intensity of •OH was obvious lower than that of $MnCO_3$@Te + $H_2O_2$+X-Ray, indicating X-Ray irradiation can promote the $MnCO_3$@Te to generate •OH (Fig. 2f and g). Electron spin resonance (ESR) further demonstrated that the characteristic peak intensity of •OH was highest for $MnCO_3$@Te + X-Ray + $H_2O_2$ groups, which was consistent with MB analysis (Fig. 2h). Meanwhile, we employed 1,3-diphenyl-isobenzofuran (DPBF) probe to monitor the overproduction of $^1O_2$ radicals induced by the combination of $MnCO_3$@Te and X-Ray irradiation in different mediums. As shown in Fig. S5, with the increase of time, the absorption of DPBF at 410 nm gradually decreased, which revealed that under the X-Ray stimulation, $MnCO_3$@Te could generate $^1O_2$ radicals. We also found that in the environment containing $H_2O_2$, $MnCO_3$@Te exhibited a much higher oxidation rate compared with pH5.3 PBS solution. Above results commonly indicated that $MnCO_3$@Te was mainly stimulated by the Fenton-like reaction to produce free radicals. Subsequently, cellular ROS level was examined qualitatively and quantitatively with dihydroethidium (DHE) as a probe. As expected, for the four groups (Control, X-Ray, $MnCO_3$@Te, $MnCO_3$@Te + X-Ray), the gradual increase in red fluorescence reveals more generation of ROS (Fig. 2i and j). Besides, increased evidence showed semiconductor heterostructures can promote the separation of $h^+$-$e^-$ pairs and then improve the catalysis ability to produce ROS. According to literature reported [38,41], the valence band (VB) and conduction band (CB) of $MnCO_3$ semiconductor were 2.43 eV and −0.82 eV, which could oxidize $H_2O$ to form •OH ($E_{H2O/\bullet OH}$ = 1.99 eV) and stimulate the transition of $O_2$ to $\bullet O_2^-$ ($E_{O2/\bullet O2-}$ = −0.33 eV). The VB and CB of TeNDs with narrow band gap semiconductor were 0.72 eV and −0.23 eV. The above results proved the between $MnCO_3$ and TeNDs is easy to form heterojunction to promote ROS production (Fig. 2a). All these results showed that $MnCO_3$@Te have good ability and probably used to sensitized tumor radiotherapy by mediating the excessive generation of ROS.

The metabolism and transformation of Te nanomedicine in the body directly affect its toxicity, which is a scientific issue worthy of in-depth exploration. Hence we introduced high-resolution mass spectrometry (HR-MS) to detect the potential metabolites of TeNDs in the medium of GSH *in vitro*. As shown in Fig. S6, after mixing TeNDs and GSH, the GSSG peak increased obviously and a new GSTeSG peak appeared. The results indicated that Te nanomaterials may be metabolized as metabolic intermediates of GSTeSG in the body, which was consistent with the previous results [55].

Moreover, it is widely known that $Mn^{2+}$ with five unpaired electrons is an effective T1 contrast agent in MR imaging [56]. To confirm the MR contrast capabilities, we used 3.0-T clinical MR scanner to capture the MR imaging of $MnCO_3$@Te incubated in buffer solutions with different pHs. As presented in Fig. 2k-l, from the T1 MR imaging, the significant concentration-dependent brightening effect of $MnCO_3$@Te were observed. Importantly, the relaxation rate of $MnCO_3$@Te at pH7.4 buffer was 1.801 $mM^{-1}s^{-1}$, while the relaxation rate was measured to be 2.645 $mM^{-1}s^{-1}$ after incubation in pH 5.3 solution. Meanwhile, after the injection of $MnCO_3$@Te into the tumor of mice, decreased T1 signal intensity was observed in the tumor tissue, which also confirmed the feasibility of MRI *in vivo* (Fig. S7). Furthermore, the generation $CO_2$ gas induced by $MnCO_3$@Te can be used as ultrasound imaging agent [57]. As expected, the $MnCO_3$@Te showed obvious imaging signal in the pH = 5.3 solution (Fig. 2m-n). These results proved that $MnCO_3$@Te can act as a good MRI and ultrasound contrast agent to guide tumor treatment at specific tumoral acidic pH.

### 2.3. Synergistic radiosensitization effects between $MnCO_3$@Te and X-Ray in vitro

Encouraged by excellent ROS generation ability of $MnCO_3$@Te, we next evaluate the anticancer efficacy and radiosensitization effects of $MnCO_3$@Te in breast cancer cells (4T1 and MDA-MB-M231) by 3-(4,5-dimethylthiazol-2-yl)-2,5-diphenyltetrazolium bromide (MTT) method. Firstly, without X-Ray irradiation, the viabilities of $MnCO_3$@Te, $MnCO_3$ and TeNDs with different concentrations were showed in Fig. 3a–c. As a results, TeNDs did not exhibit notable toxicity to 4T1 and MDA-MB-M231 cells even at the concentration of 50 mg/L, but $MnCO_3$ and $MnCO_3$@Te displayed concentration dependent cytotoxicity toward 4T1 and MDA-MB-M231 cells, reflecting the high antitumor activity of Mn-based nanosystems. Notably, the result of isobologram analysis showed the anticancer efficacy between TeNDs and $MnCO_3$ on 4T1 and MDA-MB-M231 cells was synergetic effect, as evidenced by the location of the data points far below the line defining additive effect (Fig. S8). Moreover, it was found that the cell viabilities and $IC_{50}$ value of 4T1 and MDA-MB-M231 cells further decreased after incubation with

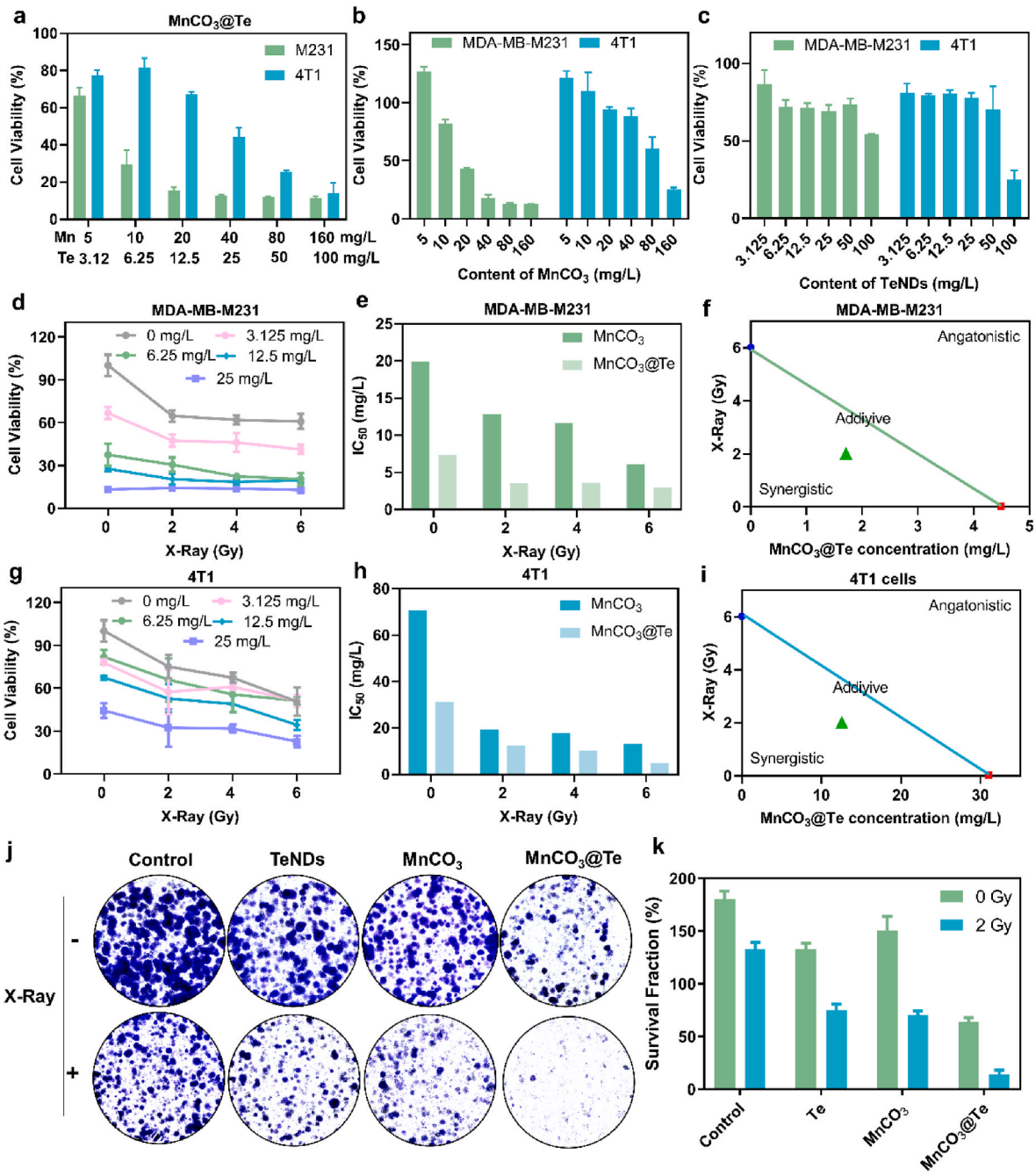


**Fig. 3. Synergistic effects of $MnCO_3$@Te and X-Ray on killing breast cancer cells.** Without X-Ray irradiation, cell viabilities of MDA-MB-M231 and 4T1 cells treated with different concentrations of $MnCO_3$@Te (a), $MnCO_3$ (b) and TeNDs (c). With different dosage of X-Ray irradiation, cell viabilities of MDA-MB-M231 (d) and 4T1 cells (g) treated with different concentrations of $MnCO_3$@Te (calculated by Te). $IC_{50}$ value of $MnCO_3$ and $MnCO_3$@Te (calculated by Mn) with or without X-Ray on MDA-MB-M231 cells (e) and 4T1 cells (f) after 72 h-incubation. Isobologram analysis of the synergistic antitumor effects of $MnCO_3$@Te combined with X-Ray in MDA-MB-M231 (f) and 4T1 (i) cells. (j–k) Representative photographs of stained colonies of MDA-MB-M231 cells treated with PBS, PBS + X-Ray, TeNDs, TeNDs + X-Ray, $MnCO_3$, $MnCO_3$+X-Ray, $MnCO_3$@Te and $MnCO_3$@Te + X-Ray after 7 days.

$MnCO_3$@Te followed by X-Ray irradiation (Fig. 3d and e and 3g-h). In specific, the $IC_{50}$ values of the combination treatment of $MnCO_3$@Te and X-Ray (2 Gy, 4 Gy and 6 Gy) toward 4T1 cells were 12.583, 10.332, and 4.842 mg/L, respectively, obviously superior to bare $MnCO_3$@Te (31.023 mg/L). In addition, we also carried out isobologram analysis to examine the connection between $MnCO_3$@Te and X-rays. As expected, the synergistic effect could be found in both 4T1 cells and MDA-MB-M231 cells (Fig. 3f and i). Finally, $MnCO_3$@Te also inhibited the colony formation of MDA-MB-M231 cells after X-ray radiation at a significantly higher level than TeNDs and $MnCO_3$ (Fig. 3j and k). Taken together, $MnCO_3$@Te mediated good radiosensitization effect and hold a good application prospect in reversing radioresistance at the cellular level.

### 2.4. *Action mechanism of $MnCO_3$@Te cooperating with radiotherapy for killing cancer cells*

The intracellular mechanism of synergistic effect of $MnCO_3$@Te and radiotherapy on killing tumor cells was evaluated by confocal fluorescence imaging and flow cytometry. Generally, anticancer effect of the nanosystem prerequisites its effective cellular uptake, thus, we analyzed

the cellular uptake of $MnCO_3$@Te with different concentrations in different incubation times. The results in Fig. 4a and b showed $MnCO_3$@Te could rapidly enter tumor cells and continuous increased with incubation time prolonged. Since the damage of mitochondria and DNA caused by ROS produced in cancer cells is the main reason for X-rays to kill cancer cells, thus we further carried out γ-H2AX detection and mitochondrial determination to explain the mechanism of $MnCO_3$@Te sensitizing X-ray [58]. We could observe from Fig. 4c that $MnCO_3$@Te + X-ray group induced largest number of fluorescent spots of γ-H2AX, which reflected the most serious DNA damage. Consistently, western blotting results (Fig. S9) also showed $MnCO_3$@Te + X-ray group induced the strongest DNA damage. In addition, Mito-tracter and Hoechst 33342 probes were used to label mitochondria and nucleus of MDA-MB-231 cells. For cells treated with X-Ray/$MnCO_3$@Te alone, only slight fragmentation could be observed. In contrast, when X-ray was used simultaneously, $MnCO_3$@Te caused scattered visual spots throughout cytoplasm (Fig. 4d). Moreover, JC-1 fluorescent probe was used to measure mitochondrial membrane potential (ΔΨm). Consistent with the above results (Fig. 4d), compared with X-Ray group, the percentage and intensity of ΔΨm with J-aggregate was significantly increased in the $MnCO_3$@Te + X-Ray group (Fig. 4e and f). Furthermore, to explore the death mode of MDA-MB-231 cells induced by $MnCO_3$@Te and X-Ray, PI staining and Annexin V-FITC/PI double staining assay were performed. As shown in Fig. 4g–i, apoptosis and S-phase arrest were the main mode of cell death caused by $MnCO_3$@Te and X-Ray in combination. For example, when concentration of $MnCO_3$@Te was 100 μM, under X-Ray radiation, the total apoptosis rate of MDA-MB-231 cells was 62.33%, higher than that of bare $MnCO_3$@Te (44.64%) and X-Ray (13.48%). PARP are vital characteristic hallmarks of apoptosis of cell apoptosis. The results (Fig. S9) showed treatment with $MnCO_3$@Te combined with X-Ray activated the proteolytic cleavage of PARP, further confirming the important role of apoptotic in $MnCO_3$@Te-induced cell death. Overall, the mechanism of cell death revealed that $MnCO_3$@Te cooperating with radiotherapy triggered ROS overproduction in cancer cells and then caused DNA damage and mitochondrial dysfunction, thereby inducing cancer cell cycle arrest and apoptosis to kill cancer cells.

### 2.5. *Immune activation effect of $MnCO_3$@Te nanosystem based on STING pathway*

The latest results have indicated that $Mn^{2+}$ play an key role in immune activation, which can serve as a potent STING agonist to effectively promote the maturation of DCs and the polarization of M1 macrophages [59,60]. Hence, we evaluated the effects of the $MnCO_3$@Te nanosystem on the immune activation by introducing a series of experiments *in vitro* (Fig. 5a). Firstly, we extracted bone-marrow-derived macrophages (BMDMs) and bone marrow-derived dendritic cells (BMDCs) from BALB/c mice. Then, the abilities of $MnCO_3$@Te nanosystem to activate DC maturation and induce macrophage repolarization were investigated by flow cytometry. As shown in Fig. 5b and c and 5e-f, compared with PBS group, there were no obvious changes in the percentage of matured DCs (CD11c + $CD80^+CD86^+$) and M2-type macrophage (CD11b + F4/80+CD206+) in TeNDs group, indicating that the TeNDs had little effect on immune activation. Notably, the treatment of $MnCO_3$@Te significantly increased the level of matured DCs from 28.3% to 50.21% and decreased the percentage of M2 macrophage from 69.3% to 46.69%, both of which

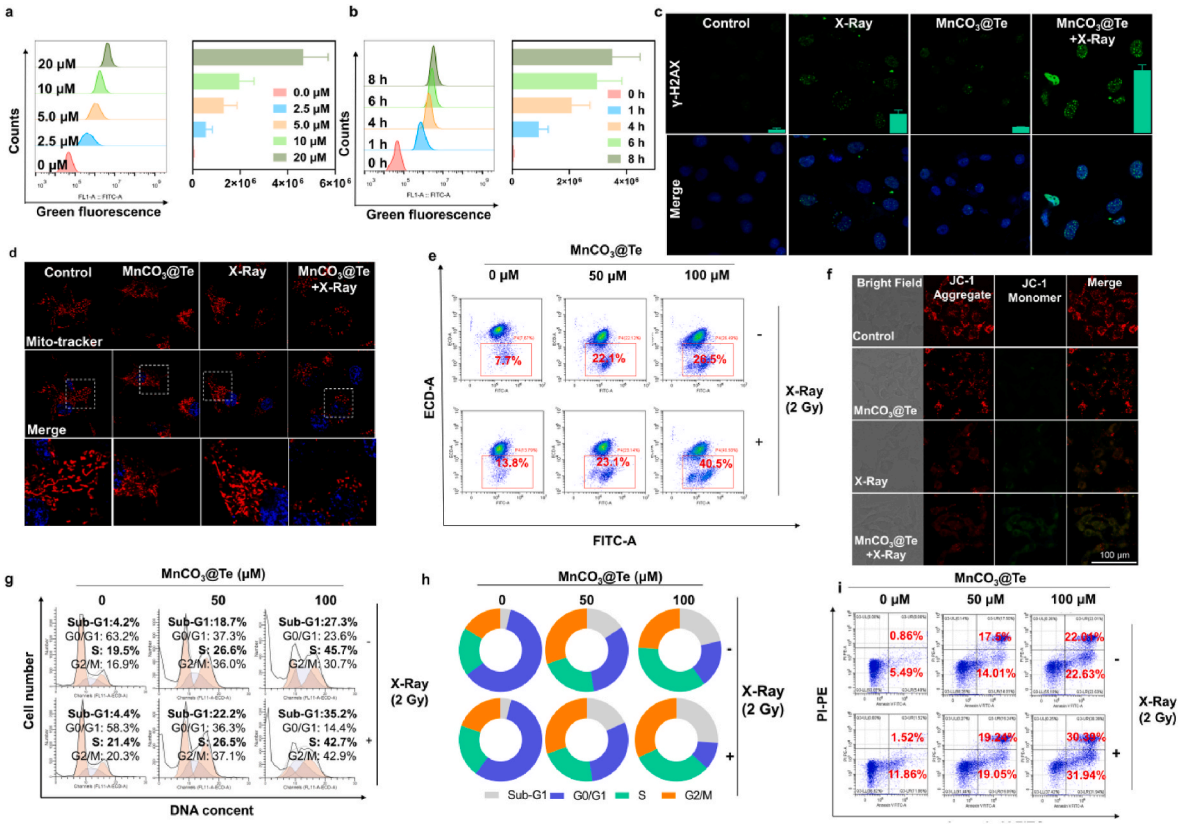


**Fig. 4. Anticancer action mechanism of combination treatment of $MnCO_3$@Te and X-Ray to MDA-MB-231 cells.** (a–b) Cellular uptake of different concentrations $MnCO_3$@Te for different time points, determined by flow cytometry. (c) Representative fluorescence images of DNA fragmentation of MDA-MB-231 cells treated with $MnCO_3$@Te and X-ray radiation. (d) Representative images of mitochondrial dysfunction caused by $MnCO_3$@Te and X-ray radiation. (e–f) JC-1 assay for illustrating the depletion of mitochondrial membrane potential in MDA-MB-231 cells treated with $MnCO_3$@Te and then X-Ray irradiation. (g–h) Flow cytometric analysis of the cell cycle of MDA-MB-231 cells after introduction $MnCO_3$@Te with or without X-rays (2 Gy). (i) Annexin V-FITC/PI staining kit detected the apoptosis of MDA-MB-231 cells treated with $MnCO_3$@Te followed by X-Ray exposure.

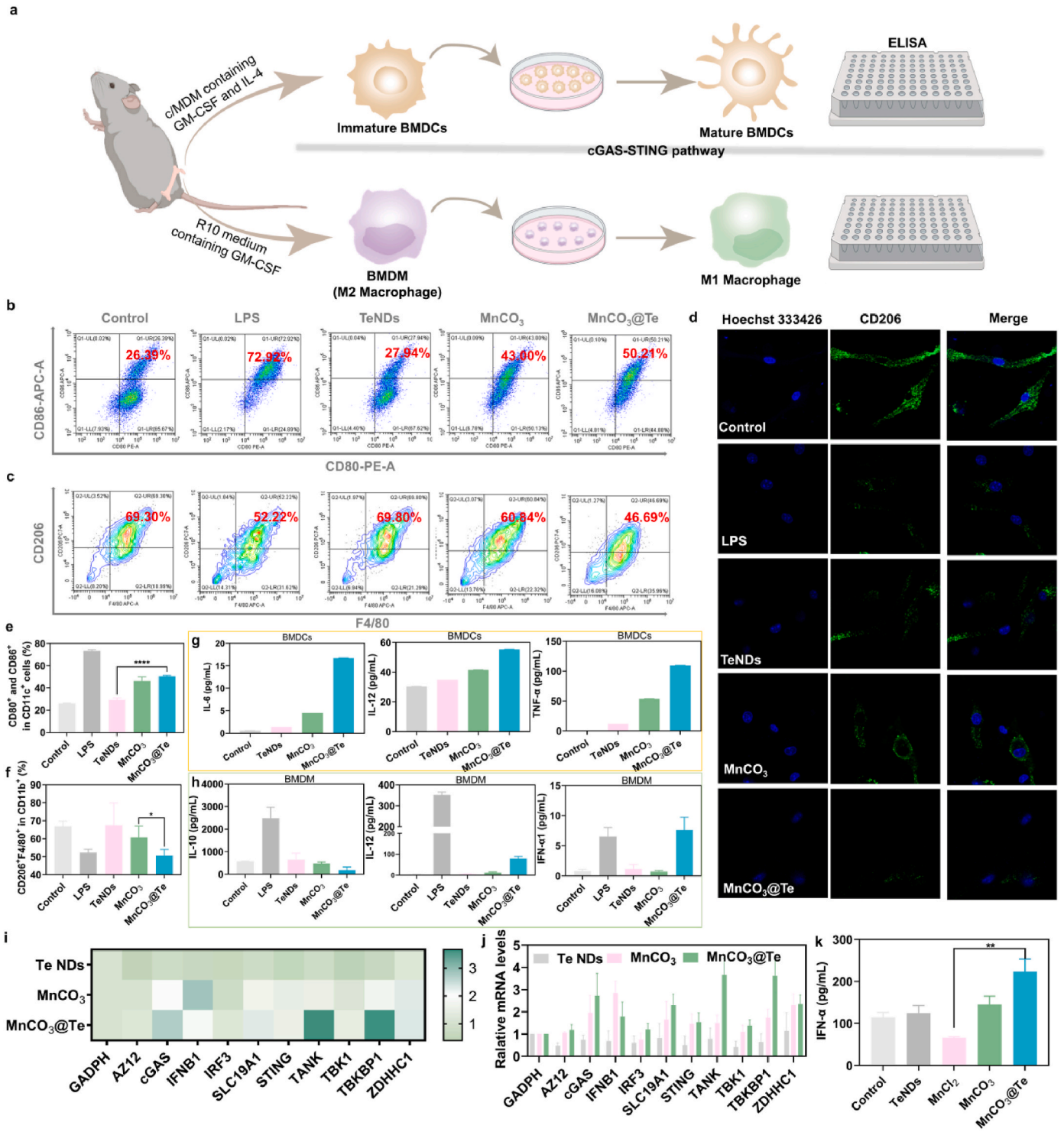


**Fig. 5. $MnCO_3$@Te as immunomodulator to promote immune activation effect via STING pathway.** (a) Schematic illustration of experimental design for detection of DC maturation and macrophage M1 repolarization. (b, e) Representative flow cytometry images and its corresponding statistical data of mature DCs (CD11c + $CD86^+CD80^+$, gated on CD11c + cell) after different treatment for 12 h. (c, f) Representative images and statistical data to show the M2-type tumor-associated macrophage (CD11b + F4/80+CD206+, gated on CD11b+). (d) Confocal fluorescence images of CD206 stained-DC2.4 cells after treatment with PBS, LPS, TeNDs, $MnCO_3$ and $MnCO_3$@OVA for 12 h. Related cytokines expression secreted by BMDCs (g) and BMDMs (h) in the medium after treatment with different conditions for 12 h. (i–j) qPCR analysis to examine the relative gene expression of cGAS-STING in BMDCs with different treatments for 24 h. (k) IFN-α level in the culture supernatant of BMDCs after different treatments.

were better than the single $MnCO_3$ nanosystem. Meanwhile, the results of CD206 immunofluorescence in BMDMs further proved that $MnCO_3$@Te could promote the polarization of macrophages (Fig. 5d). Moreover, relevant cytokines secreted by BMDCs and BMDMs have also been changed to a certain level (Fig. 5g and h).

Furthermore, we would like to investigate the ability of $MnCO_3$@Te to activate the cGAS-STING pathway by real-time quantitative PCR (RT-qPCR) assay. As shown in Fig. 5i and j, $MnCO_3$@Te group trigger the

expression of cGAS-STING axis genes in BMDCs, which was much stronger than TeNDs and $MnCO_3$ groups. Additionally, Enzyme-linked immunosorbent assay (ELISA) assay revealed $MnCO_3$@Te nanovaccine potently enhanced the expression levels of cytokines of IFN-α in the culture supernatant of treated BMDCs. Taken together, these findings argued that MnCO3@Te could promote DCs maturation through the activation of cGAS-STING pathway, and induce the secretion of type I IFN, which may be indispensable for the activation of adaptive immunity against tumors.

### 2.6. *In vivo anticancer effects of $MnCO_3$@Te evaluation by remodeling immuno-microenvironment*

After confirming the immunostimulating efficacy *in vitro*, we next evaluated the antitumor effect of the $MnCO_3$@Te-based radiotherapy combined with anti-PD-L1 checkpoint blockade *in vivo*. Here, we established BALB/c orthotopic breast tumor model with 4T1 cells. According to the regime in Fig. 6a, the mice were randomized into five groups: (1) PBS, (2) X-Ray, (3) $MnCO_3$@Te, (4) $MnCO_3$@Te + X-Ray and (5) $MnCO_3$@Te + X-Ray + anti-PD-L1. Then, on the first and third days of treatment, mice were injected with $MnCO_3$@Te intratumorally. Then, on the second and the fourth days, the mice received radiotherapy (2 Gy) and immunotherapy (anti-PD-L1). Firstly, during the treatment, the body weight of mice did not change significantly, suggesting biosafely of $MnCO_3$@Te in tumor treatment (Fig. 6b). The therapeutic efficacy was presented in Fig. 6c–g. As expected, these results of tumor weight, tumor volume and of tumor growth curves commonly demonstrated that the tumor growth in $MnCO_3$@Te + X-Ray + anti-PD-L1 group was most significantly inhibited, followed by $MnCO_3$@Te + X-Ray group. For example, tumor weight after dissection in $MnCO_3$@Te + X-Ray group at 21 days of treatments was 0.90 g, much lower than that of X-ray treatment (1.69 g) and $MnCO_3$@Te (1.37 g), reflecting that the excellent radiosensitization ability of $MnCO_3$@Te *in vivo* (Fig. 6c). Correspondingly, no obvious necrosis could be observed in the hematoxylin and eosin (H&E) staining of tumor slices from the mice treated with PBS or X-Ray. However, combined treatment of radiotherapy and immunotherapy based on $MnCO_3$@Te caused serious cell necrosis and hemorrhagic inflammation (Fig. 6g). Moreover, survival rate of mice was assessed over the course of 30 days. As shown in Fig. S10, the group of control and free $MnCO_3$@Te exhibited 33.3% and 35.5% of survival, while the (4) and (5) groups remains 81.8% and 77.9% within 30 days. The results showed our developed "$MnCO_3$@Te + X-Ray" and "$MnCO_3$@Te + X-Ray + anti-PD-L1" combination strategy could enhance the survival of tumor-bearing mice than single modality. Taken together, $MnCO_3$@Te helps to enhance the sensitivity of tumor cells to X-rays and achieve the synergistic effect of radiotherapy and immunotherapy.

It is well known that TME is immunosuppressive, which may largely

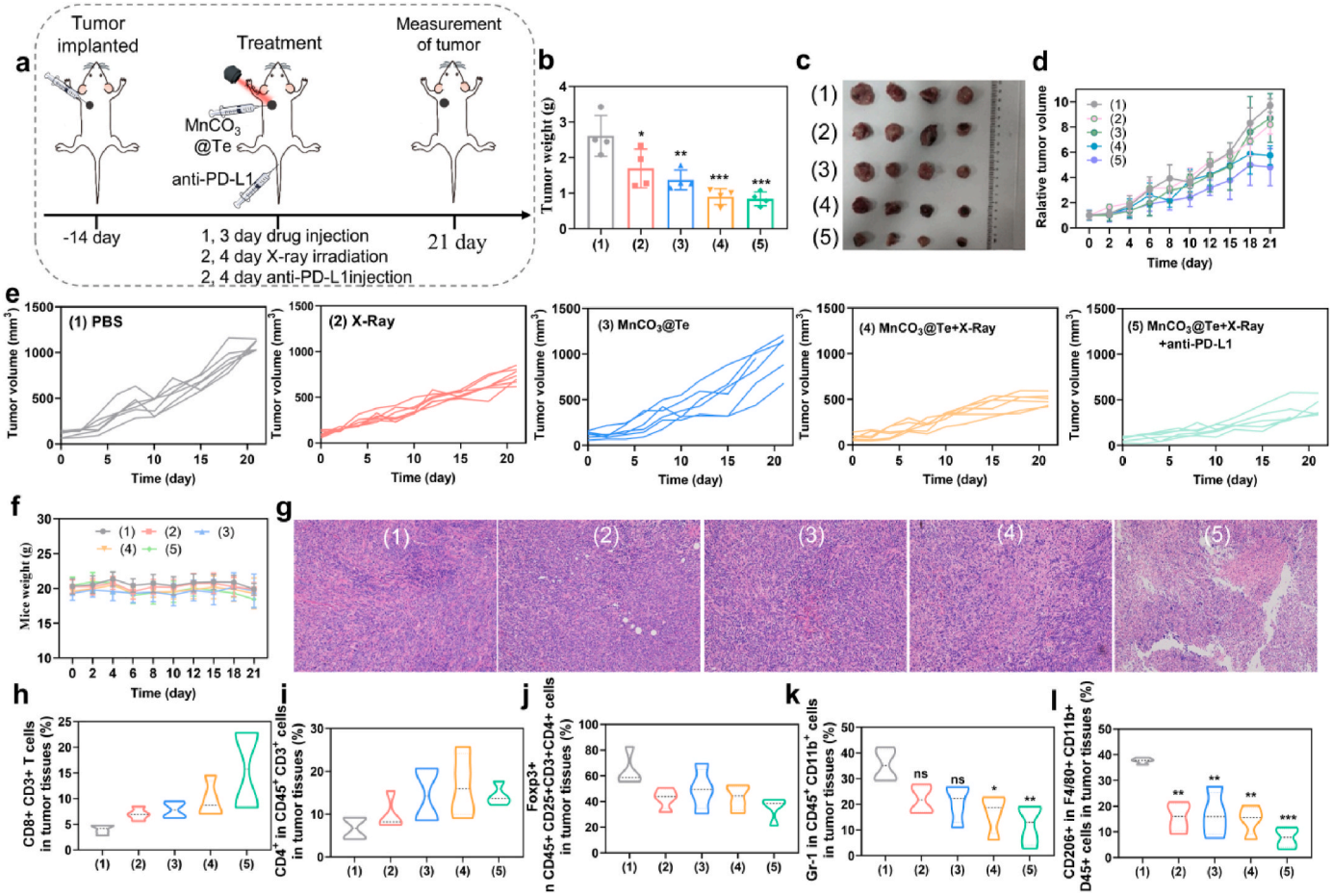


**Fig. 6. Anticancer immunity of $MnCO_3$@Te-mediated radiotherapy in combination of anti-PD-L1 *in vivo*.** (a) Schematic illustration showing the experiment design using $MnCO_3$@Te-based RT and anti-PD-L1 to treat mice bearing 4T1 tumors. (b) Average tumor weight of various groups after treatment. (c) Photographs of tumors excised from Balb-c mice. (d) Relative tumor growth curves in different treatment groups. (e) Growth curves of tumor volume for individual Balb-c mice following various treatments. (f) Mice weight changes within treatment period. (g) H&E-stained images of tumor tissues collected from mice post various treatments. Quantification analysis of the infiltration of T lymphocytes including $CD8^+CD3^+$ T cells (h) and $CD3^+CD4^+$ T cells (i) after various treatments. Quantification analysis of decline of intratumoral immunosuppressive cells including Treg cells (j) and MDSC cells (k) in tumor tissues. (l) Flow cytometry analysis of the proportion of M2-phenotype tumor associated macrophages within tumor tissues from different immunized mice.

offset the impact of anti-tumor immunity [61]. Thus the influence of $MnCO_3$@Te on the tumor immuno-microenvironment was explored to uncover the mechanisms underlying the observed antitumor efficacy. Firstly, we soaked Mn in an acidic environment with pH = 5.3, and found that the pH value of the solution gradually increased, close to that of normal tumor tissue, demonstrating $MnCO_3$@Te has the potential to neutralize acidic TME (Fig. S11) The infiltration of immune cells including CTLs, $CD4^+$ helper T lymphocytes, MDSCs, Tregs and M2-like macrophage in the tumor sites was measured using a subset of the tested mice on day 21. Firstly, the levels of $CD3^+CD8^+$ CTL cells and the $CD3^+CD4^+$ helper T cells in the $MnCO_3$@Te + X-Ray + anti-PD-L1 group were significantly increased to 15.66% and 14.27% compared with the controls (Fig. 6h–i and Fig. S12). Meanwhile, immunofluorescence staining of tumor slices from different treatment groups was carried out. As shown in Fig. S13, green ($CD8^+$ T cells) fluorescence of $MnCO_3$@Te and X-Ray plus anti-PD-L1 group were significantly stronger than that of other groups, which ultimately in line with the results of flow cytometry. Therefore, the combined radiotherapy and immunotherapy with synthesized MnCO3@Te can trigger infiltration of CTLs in tumor tissues, thus triggering immune responses. In addition to immune-activated cells, M2-phenotype macrophages, MDSCs and Tregs were the typical immunosuppressive cells in TME. The results showed the frequency of M2-phenotype macrophages, M2-MDSCs and Tregs in mice received $MnCO_3$@Te + X-Ray + anti-PD-L1 treatment was significantly lower than control and X-Ray groups (Fig. 6j-l and Fig. S12). Overall, the combination of radiotherapy and immunotherapy based on $MnCO_3$@Te could induce strong antitumor immunity and remodel immuno-microenvironment.

### 2.7. $MnCO_3$@Te-mediated radiotherapy and anti-PD-L1 combination therapy prevent lung metastasis

Tumor metastasis is the main cause of high tumor mortality, and it is also a challenge for clinical tumor treatment [62]. As one of the most invasive cancers, breast cancer is most likely to metastasize to lung tissues through circulatory system with epithelial-mesenchymal transformation [63,64]. Hence to explore the ability to prevent lung metastasis, according to the experimental design in Fig. 7a, after primary tumor generation, mice were intravenous injected 4T1 cells to build lung metastatic tumor model. First of all, the therapeutic effect of 4T1 tumor-bearing mice on primary tumors after various treatments was consistent with the above tumor model (Fig. 7b–d). After 21 days of treatment, mice were dissected and their lung tissues were taken out, fixed, stained with ink. Finally, the number of nodules on the surface of lungs were counted. As shown in Fig. 7e–f, a large number of lung metastases were seen in PBS group. Importantly, the most significant reduction in the number of lung lesions was observed in the fifth combined treatment group. Correspondingly, the results of H&E staining of lung slices were consistent with those observed in lung photographs (Fig. 7g). These results revealed that combination treatment with $MnCO_3$@Te + X-Ray + anti-PD-L1 was much more effective in preventing lung metastasis than $MnCO_3$@Te or X-Ray alone. Based on those result, we concluded that the therapeutic strategy using $MnCO_3$@Te combined with X-Ray and anti-PD-L1 has the advantage of preventing

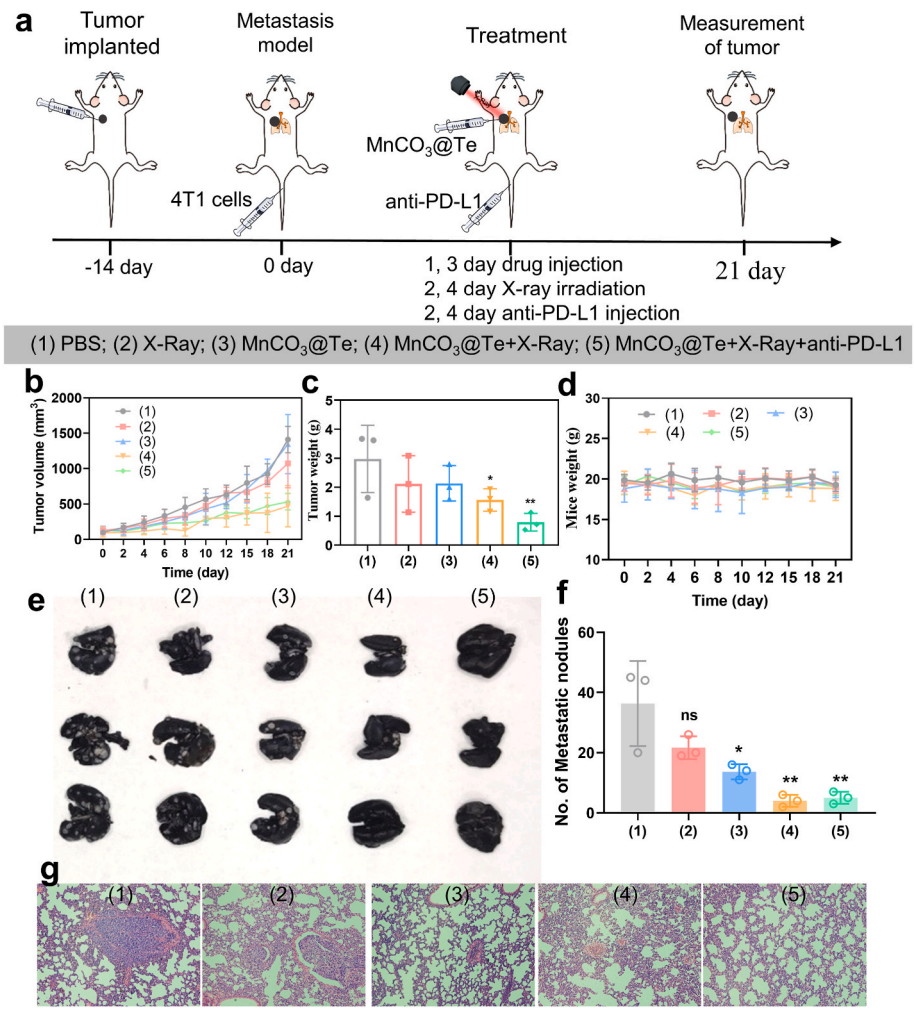


**Fig. 7. $MnCO_3$@Te-based radiotherapy in combination with aPD-1 for boosting antimetastasis activity.** (a) Schematic of the experimental procedure of $MnCO_3$@Te combined with X-Ray and anti-PD-L1 on metastatic melanoma model. (b) Tumor growth curves from different group. (c) Tumor weight profiles of each group at the 21st day post treatment. (d) Mice weight changes within treatment period. (e) Images of metastatic nodules in lungs after different treatments. (f) The quantification of metastatic nodules in lungs after different treatments. (g) H&E-stained images of lung tissues collected from mice post various treatments.

tumor metastasis, which probably attributed to the strong systemic immune response.

Metabolism and toxic side effects of nanomedicines are another key issue of concern to researchers except its anticancer effect. Firstly, we performed pharmacokinetics analysis of $MnCO_3$@Te to quantify the metabolism behavior. After intravenous injection (i.v.) of the $MnCO_3$@Te, plasma concentration of Te from mice in different group at various times were examined by inductively coupled plasma mass spectrometry (ICP-MS). As shown in Fig. S14, the plasma concentration of $MnCO_3$@Te gradually decreased with time. In an analysis of pharmacokinetic parameters, we found $MnCO_3$@Te exhibited an elimination half-life ($t_{1/2\beta}$) of 36.59 h and area under the curve of 214.32 μg/mL*h, which was higher than that of TeNDs reported in previous literature [38]. The results confirmed that the packaging of $MnCO_3$ nanosystem helps to improve and prolong the blood circulation life of TeNDs. Furthermore, we carried out H&E staining of major organs of mice to analysis their status and then confirm biosafely. As shown in Fig. S15, obvious tumor metastasis could be observed in the liver tissues in the groups treated PBS, X-Ray and $MnCO_3$@Te. However, the slices of major organs including heart, liver, spleen and kidney could hardly detect obvious inflammation or other pathological change induced by $MnCO_3$@Te nanosystems even after the X-Ray irradiation plus anti-PD-L1 treatment, which verified its high safety and low toxicity as agonist.

## 3. Conclusion

An increasing number of studies found radiotherapy is closely associated with immune system in the treatment of breast cancer. Thus the combination of radiotherapy and immune checkpoint therapies have received considerable attention in the application of various tumor therapies. However, radioresistance and immunosuppression in TME have limited its therapeutic effectiveness across patients. Therefore, it is urgent to develop a nanoplatform to simultaneous overcome radioresistance and reprogram tumor immune microenvironment, so as to realize the efficient combination of radiotherapy and immunotherapy. Hence, in this work, we successfully designed and developed a Te-directed maple leaf $MnCO_3$ nanotherapeutics for the radio-immunotherapy of cancer to inhibit tumor progression and lung metastasis.

In detail, the conclusions can be summarized as follows. (a) The reasonable design of $MnCO_3$ wrapped Te greatly affects the diameter and morphology of $MnCO_3$ crystal, including the transformation from spherical to maple leaf to rod. (b) $MnCO_3$ nanomaterials can release a large number of $Mn^{2+}$ and react with $H_2O_2$ to generate free radicals such as •OH under the acidic environment of tumor, therapy realizing the anti-tumor activity of CDT through changing the fenton-like reaction of Mn valence. (c) $MnCO_3$@Te exhibits excellent radiosensitization efficacy by inducing cellular apoptosis and mitochondrial fragmentation, which was higher than Te/$MnCO_3$ alone. (d) Increased the pH value of TME to create a favorable environment for immune activation, realizing strong inhibitory efficacy on the tumor growth containing primary tumor and metastatic tumor. Overall, our study not only provides a facile way to synthesize different morphology $MnCO_3$ systems but also highlights the potential of $MnCO_3$@Te as radiosensitizers and immunomodulator for the therapy of breast cancer lung metastases by combining with immunotherapy.

## 4. Experimental section

### 4.1. Materials

Manganese chloride tetrahydrate ($MnCl_2$•$4H_2O$), ammonium bicarbonate ($NH_4HCO_3$), sodium tellurite ($Na_2TeO_3$), sodium borohydride ($NaHB_4$), BSA, phosphate-buffered saline (PBS), DMEM medium, fetal bovine serum (FBS) and paraformaldehyde were purchased from Sigma. propidium iodide (PI) and Mito-Tracker Red were purchased from Thermo Fisher Scientific. All flow cytometric antibodies were obtained from Biolegend. Anti-PD-L1 monoclonal antibody was purchased from Neobioscience. Ultrapure water used in the experiments was supplied by a Mili-Q water purification instrument from Millipore.

### 4.2. Preparation of TeNDs

TeNDs was obtained based on previous explorations [38]. In detail, 25 mg/mL BSA (10 mL) was mixed with 20 mM $Na_2TeO_3$ (2 mL) under mild stirring. Then, adjust the pH value of the above mixed solution to 10–12 with NaOH solution. Subsequently, $NaHB_4$ with a concentration of 100 mM was quickly added to the above mixed solution for reaction 4 h at 50 °C. Finally, the acquired solution was dialyzed against Milli-Q water for 24 h using a dialysis bag (50000 Da).

### 4.3. Preparation of $MnCO_3$@Te nanotherapeutics

The solution of 1 mL $MnCl_2$•$4H_2O$ (6.25 mg/mL) and TeNDs (4 mL) was mixed and placed into an airtight container containing ammonium bicarbonate, reacted for 1.5 h until the solution appeared obvious turbidity. The material was obtained after washing three times by centrifugation (12000 rpm) with ultrapure water. Meanwhile, to analysis the formation progress of maple leaf-shaped $MnCO_3$@Te nanotherapeutics, we changed the synthesis time in the reaction system under other unchanged conditions. In addition, we also prepared $CaCO_3$@Te nanotherapeutics with the synthesis strategy of $MnCO_3$@Te by using $CaCl_2$ to replace $MnCl_2$•$4H_2O$.

### 4.4. Characterization of $MnCO_3$@Te nanotherapeutics

The structure and chemical composition of the prepared $MnCO_3$@Te were characterized by high resolution transmission electron microscope (HRTEM, JEM-2100) equipped with energy-dispersive X-ray spectroscopy (EDS), field emission scanning electron microscope (FESEM, ULTRA-55), X-ray diffraction (XRD, miniflex 600) and X-ray photoelectron spectroscopy (XPS, Thermo Scientific K-Alpha+). The size distribution and zeta potential of nanomaterials were characterized by using Zetasizer Nano ZS particle analyzer (Malvern Instruments Limited). Concentration of the $MnCO_3$@Te were determined by inductively coupled plasma mass spectrometry (ICP-MS, Thermo UltiMate 3000+iCAP RQ). Meanwhile, in order to explore the formation process of the nanosystem, the changes in $MnCO_3$@Te morphology at different reaction times were characterized by HRTEM.

### 4.5. Response performance of $MnCO_3$@Te nanotherapeutics

To detect the acid sensitivity of nanomaterials, $MnCO_3$ and $MnCO_3$@Te were placed in PBS solution with pH = 7.4 and pH = 5.3, respectively. Then, the morphology changes of $MnCO_3$ and $MnCO_3$@Te in an acidic environment for 6 h, 12 h, and 24 h were obtained from the transmission electron microscopy. Meanwhile, the content of Mn in the supernatant after centrifugation was detected by ICP-MS to understand the decomposition of the $MnCO_3$ and $MnCO_3$@Te.

### 4.6. MR imaging and ultrasound imaging

To evaluate the MR imaging effect of the $MnCO_3$ and $MnCO_3$@Te, we scanned MR imaging of the $MnCO_3$@Te sample dispersed in pH 7.4 and 5.3 conditions at various concentrations. Meanwhile, *in vivo* MR imaging preformed on 4T1 tumor-bearing BALB/c mice before and after administration with $MnCO_3$@Te, which were detected on 3.0T clinical MRI scanner. Moreover, ultrasound imaging *in vitro* of $MnCO_3$@Te at different concentrations was performed after incubation in acid environment (pH = 5.3).

### 4.7. Generation of reactive oxygen species

Methylene blue (MB) was mixed with $MnCO_3$@Te nanomaterial containing 10 mM $H_2O_2$ followed by X-Ray irradiation 2 Gy. Then, the sample was scanned at 500–750 nm with a UV–vis spectrophotometer to prove the •OH generation. Meanwhile, the absorbance value at 670 nm under different conditions was measured to evaluate the yield of •OH. In addition, the •OH induced by $MnCO_3$@Te were detected by ESR technique by using DMPO capture agent (A300, Bruker). The detection of •OH produced by $MnCO_3$@Te combined with X-ray and $H_2O_2$ was similar to those measured above. Similarly, DPBF probe was introduced to monitor the overproduction of $^1O_2$ radicals.

The level of intracellular ROS produced by $MnCO_3$@Te and X-Ray was detected by DHE fluorescent probe, and the fluorescence intensity changes were photographed by fluorescence microscope (EVOS), the absorbance (510 nm) of DHE in the culture medium was measured with a plate detector (cytation5, BioTek).

### 4.8. Metabolite analysis of TeNDs in vitro

Previous studies have reported that telluride could react with glutathione (GSH) *in vivo* to form trisulfide telluride (GSTeSG), and then converted to hydrogen telluride, eventually excreted from the body through methylation metabolism [55]. For this reason, we speculate whether TeNDs could produce metabolites of GSTeSG. Hence, the TeNDs were dispersed in 1 mL the buffer with GSH (10 mg/mL), followed by HR-MS detection.

### 4.9. Cell culture and cytotoxicity assays

The MDA-MB-231 cell line and the 4T1 cell line were derived from American Type Culture Collection (ATCC). In short, MDA-MB-231 and 4T1 cells were seeded in 96-well plates with 2000 cells in each well. After cell attachment, a series of concentrations of the material were incubated with the cells, and the cell survival rate was evaluated by MTT assay. At the same time, in order to study the effect of the material to enhance RT, after the material was incubated with cells, different doses of X-rays (2, 4 and 6 Gy) were used to evaluate the effect by MTT assay. In addition, the isobologram method previously described was introduced to analyze the synergy effect between $MnCO_3$@Te and X-ray.

Similarly, to evaluate the synergistic effect of $MnCO_3$@Te and X-ray on cancer cells, MDA-MB-231 cells were seeded in 6-well plates with 2000 cells per well. After cell adherence, the cells were incubated with the material and irradiated with 2 Gy of radiation for 7 days, washed lightly with PBS, and fixed with 4% paraformaldehyde. Then, the spots were stained with crystal violet and analyzed for number of spots.

### 4.10. Cellular uptake

To evaluate uptake of $MnCO_3$@Te in cells, intracellular uptake assays were performed according to the fluorescence intensity of coumarin-6-labeled $MnCO_3$@Te. MDA-MB-231 cells were incubated with $MnCO_3$@Te (2.5 μM, 5 μM, 10 μM, 20 μM) for 1 h, 4 h, 6 h, 8 h. The relative uptake of $MnCO_3$@Te was then measured by flow cytometry to obtain the cellular uptake relationship of $MnCO_3$@Te with times and concentrations.

### 4.11. Action mechanism of $MnCO_3$@Te cooperating with radiotherapy

To evaluate the damage of $MnCO_3$@Te on cancer cells, the cell cycle was analyzed by flow cytometry after labeling the cells with propidium iodide (PI) staining, and the protein expression of p-histon which associated DNA damage in the treated cells was analyzed by immunofluorescence staining and western blotting. Besides, to evaluate the apoptosis of the treated group, the apoptosis states of the cells were stained by labeling PI and annexin-V FITC dyes and analyzed by flow cytometry. Moreover, the expression level of PARP protein of MDA-MB-231 cells after different treatments was further determined by western blotting as previously described [65].

To analyze the mitochondrial damage after $MnCO_3$@Te treatment, the turnover of cell membrane potential in the drug-treated groups was evaluated by flow cytometry and fluorescence microscopy analysis of cells labeled with JC-1 fluorescent probe. The intracellular mitochondria were labeled with Mitotrack red, to analyze the mitochondrial morphology changes in the cells after drug treatment were observed by confocal fluorescence microscopy (LSM 700).

### 4.12. DC maturation, macrophage polarization, and cytokines

Bone Marrow-Derived Dendritic Cells (BMDCs) and bone marrow-derived macrophages (BMDMs) were isolated according to the method reported previously [66]. To measure the maturation of DCs induced by $MnCO_3$@Te, the isolated BMDCs were incubated with $MnCO_3$@Te, $MnCO_3$, TeNDs and LPS for 24 h, respectively, and then the cells were washed by PBS and labeled with flow antibody against CD11c, CD80, CD86, at the same time, the proportion of these antibodies in the cells was measured by flow cytometry. Similarly, the polarization of macrophages was further analyzed by flow cytometry with CD11b, F4/80 and CD206 labeled antibodies.

To further analyze the effect of $MnCO_3$@Te and $MnCO_3$ in immune cells, cytokines (IL-6, IL-12, TNF-α) in the supernatants of different treated group's BMDC were detected with ELISA kits according to vendors' protocols (obtained from Biolegend). Similarly, cytokines (IL-10, IL-12, IFN-α1) in the supernatants of different treated group's mouse BMDM were detected with ELISA kits according to vendors' protocols (obtained from Biolegend).

### 4.13. Rt-qPCR

The RT-qPCR assay was introduced to detect the gene expression of cGAS-STING in the treated cells. Briefly, the treated cells were each washed three times with cold PBS solution, total RNA was then extracted using TaKaRa MiniBEST Universal RNA Extraction Kit and transcribed to cDNA by Quantscript RT Kit (Tiangen Biotech Co., LTD, China) according to the manufacturer's instructions. Finally, qPCR assay was done using SYBR® Premix Ex Taq™ II (Takara, Japan) performed with CFX Connect™ Real-Time PCR Detection System (Bio-rad, USA) following the manufacturer's instruction. The relative gene expression was determined by the $2^{-\triangle\triangle Ct}$ method after normalization to the internal control gene of GAPDH.

### 4.14. Tumor immunotherapy in vivo

The work performed in BALB/c mice (6–8 weeks of age) was purchased from the Animal Center, Guangdong Province All animal experiments were conducted in strict accordance with national guidelines for the care and use of experimental animals and were approved by the Ethics Committee of Jinan University (Guangzhou, China) for animal experiments. $10^7$ 4T1 cells were injected into the breast of each BALB-c mice. After successful establishment of BALB/c orthotopic breast tumor model, the mice were equally divided into five groups: (1) PBS, (2) X-ray, (3) $MnCO_3$@Te, (4) $MnCO_3$@Te + X-Ray, (5) $MnCO_3$@Te + X-Ray + anti-PD-L1. Among them, the mice in group 1 and 2 were injected with PBS solution. The mice in group 3, 4 and 5 administered with $MnCO_3$@Te by intratumoral injection. In addition, the group of 2, 4 and 5 were given radiotherapy on the 2, 4 days after the administration. Anti-PD-L1 (15 μg each mouse) was administered intravenously on 2nd and 4th day. Mice weight was recorded every 2 days. The width and weight were measured with a vernier caliper, calculated by the formula (tumor volume = length × width$^2$/2), and analyzed to obtain daily maintenance detection. The relative tumor volume was calculated according to the tumor volume after treatment ($V_{day}$) divided by the tumor

volume before treatment ($V_0$). In addition, according to the feeding protocol, the mice were killed when the tumor volume was more than 1000 $mm^3$. After 21 days of treatment, the tumors were dissected, weighed and fixed for H&E staining.

### 4.15. Flow cytometry was used to analyze the infiltration of tumor immune cells

After the tumor cells were ground, the dispersed tumor cells into a single cell state were labeled with a series of flow antibodies (Tregs ($CD45^+CD3^+CD4^+CD25+FOXP3+$), MDSCs ($CD45^+CD11b$ + Gr-1+), M1-type TAM ($CD45^+CD11b$ + F4/80+CD206+), CTLs ($CD45^+CD3^+CD8^+$), Helper T Lymphocytes ($CD45^+CD3^+CD4^+$) to detect the proportion of infiltrating immune cells in the tumor cells, and the proportion of infiltrating immune cells was analyzed by flow cytometry (Antibodies were from biolegend). The $MnCO_3$@Te + X-Ray + anti-PD-L1-induced CTLs infiltration in tumor tissues was examined by immunofluorescence assay.

### 4.16. Antimetastatic activity in 4T1 tumor mice model

To evaluate the antimetastatic ability of $MnCO_3$@Te, the lung metastatic breast tumor model of BALB/c mice was established [67]. In brief, on the 14th day of primary tumor formation, $10^5$ 4T1 cells were injected from the tail vein of the mice. Then, Similar to above treatment method, mice were randomly divided into five groups and treated with PBS, PBS + X-Ray, $MnCO_3$@Te, $MnCO_3$@Te + X-Ray and $MnCO_3$@Te + X-Ray + anti-PD-L1. Finally, mice were perfused with India ink 21 days later, and the number of lung nodules on the BALB/c mice was counted. And the degree of lung metastatic from different group was evaluated by H&E staining of lung sections. Similarly, for evaluating the biosafely, H&E staining of major organs was studied.

### 4.17. In vivo pharmacokinetic assay

Female SD mice (about 200 g) were administered with $MnCO_3$@Te (0.5 mg/kg, calculated by Te) by intravenous (i.v.) injection. Then, at specific times, blood of mice in different group was collected and centrifuged to obtain plasma. The Te concentration dispersed in plasma was determined using ICP-MS.

### 4.18. Statistical analysis

All tests were conducted at least three times and all data are expressed as mean G standard deviation (SD). Statistical analysis was performed with the SPSS statistical package (SPSS 13.0 for Windows; SPSS, Chicago, IL) and differences of $p < 0.05$ (*), $p < 0.01$ (**), and $p < 0.01$ (***) were considered statistically significant.

## CRediT authorship contribution statement

**Wei Huang:** Conceptualization, Investigation, Methodology, Writing – original draft, Funding acquisition. **Sujiang Shi:** Investigation, Methodology, Writing – original draft. **Haoran Lv:** Investigation, Methodology, Writing – review & editing. **Zhenyu Ju:** Writing – review & editing. **Qinghua Liu:** Methodology, Supervision, Writing – review & editing. **Tianfeng Chen:** Conceptualization, Supervision, Funding acquisition, Writing – review & editing.

## Declaration of competing interest

The authors declare that they have no known competing financial interests or personal relationships that could have appeared to influence the work reported in this paper.

## Acknowledgments

This work was supported by National Science Fund for Distinguished Young Scholars (82225025), National Natural Science Foundation of China (21877049, 32171296, 32201166, 82172088), Guangdong Natural Science Foundation (2020B1515120043), Guangdong Basic and Applied Basic Research Fund Project (No. 2021A1515111027), and K. C. Wong Education Foundation.

## Appendix A. Supplementary data

Supplementary data to this article can be found online at https://doi.org/10.1016/j.bioactmat.2023.04.010.

## References

[1] R.L. Siegel, K.D. Miller, N.S. Wagle, A. Jemal, Cancer statistics, 2023, CA cancer, J. Clin. 73 (1) (2023) 17–48.
[2] A.N. Giaquinto, H. Sung, K.D. Miller, J.L. Kramer, L.A. Newman, A. Minihan, A. Jemal, R.L. Siegel, Breast cancer statistics, 2022, CA A Cancer J. Clin. 72 (6) (2022) 524–541.
[3] J. Marsolier, P. Prompsy, A. Durand, A.-M. Lyne, C. Landragin, A. Trouchet, S. T. Bento, A. Eisele, S. Foulon, L. Baudre, H3K27me3 conditions chemotolerance in triple-negative breast cancer, Nat. Genet. 54 (4) (2022) 459–468.
[4] R.S. Riley, C.H. June, R. Langer, M.J. Mitchell, Delivery technologies for cancer immunotherapy, Nat. Rev. Drug Discov. 18 (3) (2019) 175–196.
[5] Y. Zhang, Z. Feng, J. Liu, H. Li, Q. Su, J. Zhang, P. Huang, W. Wang, J. Liu, Polarization of tumor-associated macrophages by TLR7/8 conjugated radiosensitive peptide hydrogel for overcoming tumor radioresistance, Bioact. Mater. 16 (2022) 359–371.
[6] M. Binnewies, E.W. Roberts, K. Kersten, V. Chan, D.F. Fearon, M. Merad, L. M. Coussens, D.I. Gabrilovich, S. Ostrand-Rosenberg, C.C. Hedrick, R. H. Vonderheide, M.J. Pittet, R.K. Jain, W. Zou, T.K. Howcroft, E.C. Woodhouse, R. A. Weinberg, M.F. Krummel, Understanding the tumor immune microenvironment (TIME) for effective therapy, Nat. Med. 24 (5) (2018) 541–550.
[7] J. Wang, Y. Chang, H. Luo, W. Jiang, L. Xu, T. Chen, X. Zhu, Designing immunogenic nanotherapeutics for photothermal-triggered immunotherapy involving reprogramming immunosuppression and activating systemic antitumor responses, Biomaterials 255 (2020), 120153.
[8] Y. Chao, Z. Liu, Biomaterials tools to modulate the tumour microenvironment in immunotherapy, Nat. Rev. Bioeng. 1 (2023) 125–138.
[9] T. Wang, H. Zhang, W. Qiu, Y. Han, H. Liu, Z. Li, Biomimetic nanoparticles directly remodel immunosuppressive microenvironment for boosting glioblastoma immunotherapy, Bioact. Mater 16 (2022) 418–432.
[10] M. Yang, J. Li, P. Gu, X. Fan, The application of nanoparticles in cancer immunotherapy: targeting tumor microenvironment, Bioact. Mater. 6 (7) (2021) 1973–1987.
[11] Z. Fan, H. Liu, Y. Xue, J. Lin, Y. Fu, Z. Xia, D. Pan, J. Zhang, K. Qiao, Z. Zhang, Y. Liao, Reversing cold tumors to hot: an immunoadjuvant-functionalized metal-organic framework for multimodal imaging-guided synergistic photo-immunotherapy, Bioact. Mater. 6 (2) (2021) 312–325.
[12] Q. Dai, L. Wang, E. Ren, H. Chen, X. Gao, H. Cheng, Y. An, C. Chu, G. Liu, Ruthenium-based metal–organic nanoradiosensitizers enhance radiotherapy by combining ROS generation and CO gas release, Angew. Chem., Int. Ed. (2022), e202211674.
[13] H.H. Chen, M.T. Kuo, Improving radiotherapy in cancer treatment: promises and challenges, Oncotarget 8 (37) (2017), 62742.
[14] W. Li, J. Yan, H. Tian, B. Li, G. Wang, W. Sang, Z. Zhang, X. Zhang, Y. Dai, A platinum@polymer-catechol nanobraker enables radio-immunotherapy for crippling melanoma tumorigenesis, angiogenesis, and radioresistance, Bioact. Mater. 22 (2023) 34–46.
[15] X. Zhang, J. Tang, C. Li, Y. Lu, L. Cheng, J. Liu, A targeting black phosphorus nanoparticle based immune cells nano-regulator for photodynamic/photothermal and photo-immunotherapy, Bioact. Mater. 6 (2) (2021) 472–489.
[16] Z. Song, T. Liu, H. Lai, X. Meng, L. Yang, J. Su, T. Chen, A universally EDTA-assisted synthesis of polytypic bismuth telluride nanoplates with a size-dependent enhancement of tumor radiosensitivity and metabolism in vivo, ACS Nano 16 (3) (2022) 4379–4396.
[17] L. Chan, P. Gao, W. Zhou, C. Mei, Y. Huang, X.F. Yu, P.K. Chu, T. Chen, Sequentially triggered delivery system of black phosphorus quantum dots with surface charge-switching ability for precise tumor radiosensitization, ACS Nano 12 (12) (2018) 12401–12415.
[18] W. Jiang, Z. Zhang, M. Ye, S. Pan, G. Huang, T. Chen, X. Zhu, Morphology-directed radiosensitization of MoSe2 nanoplatforms for promoting cervical cancer radiotherapy, Nano Today 46 (2022), 101598.
[19] Y. Chao, L. Xu, C. Liang, L. Feng, J. Xu, Z. Dong, L. Tian, X. Yi, K. Yang, Z. Liu, Combined local immunostimulatory radioisotope therapy and systemic immune checkpoint blockade imparts potent antitumour responses, Nat. Biomed. Eng. 2 (8) (2018) 611–621.

[20] Q. Chen, J. Chen, Z. Yang, J. Xu, L. Xu, C. Liang, X. Han, Z. Liu, Nanoparticle-enhanced radiotherapy to trigger robust cancer immunotherapy, Adv. Mater. 31 (10) (2019), e1802228.
[21] H. Li, M. Wang, B. Huang, S.W. Zhu, J.J. Zhou, D.R. Chen, R. Cui, M. Zhang, Z. J. Sun, Theranostic near-infrared-IIb emitting nanoprobes for promoting immunogenic radiotherapy and abscopal effects against cancer metastasis, Nat. Commun. 12 (1) (2021) 7149.
[22] F.M. Howard, A.T. Pearson, R. Nanda, Clinical trials of immunotherapy in triple-negative breast cancer, Breast Cancer Res. Treat. 195 (1) (2022) 1–15.
[23] L. Xu, C. Zou, S. Zhang, T.S.M. Chu, Y. Zhang, W. Chen, C. Zhao, L. Yang, Z. Xu, S. Dong, H. Yu, B. Li, X. Guan, Y. Hou, F.M. Kong, Reshaping the systemic tumor immune environment (STIE) and tumor immune microenvironment (TIME) to enhance immunotherapy efficacy in solid tumors, J. Hematol. Oncol. 15 (1) (2022) 87.
[24] X. Qu, D. Zhou, J. Lu, D. Qin, J. Zhou, H.J. Liu, Cancer nanomedicine in preoperative therapeutics: nanotechnology-enabled neoadjuvant chemotherapy, radiotherapy, immunotherapy, and phototherapy, Bioact. Mater. 24 (2023) 136–152.
[25] C. Corbet, O. Feron, Tumour acidosis: from the passenger to the driver's seat, Nat. Rev. Cancer 17 (10) (2017) 577–593.
[26] J. Ling, Y. Chang, Z. Yuan, Q. Chen, L. He, T. Chen, Designing lactate dehydrogenase-mimicking SnSe nanosheets to reprogram tumor-associated macrophages for potentiation of photothermal immunotherapy, ACS Appl. Mater. Interfaces 14 (24) (2022) 27651–27665.
[27] K. Khalaf, D. Hana, J.T.-T. Chou, C. Singh, A. Mackiewicz, M. Kaczmarek, Aspects of the tumor microenvironment involved in immune resistance and drug resistance, Front. Immunol. 12 (2021), 656364.
[28] Y. Zhou, T. Ye, C. Ye, C. Wan, S. Yuan, Y. Liu, T. Li, F. Jiang, J.F. Lovell, H. Jin, J. Chen, Secretions from hypochlorous acid-treated tumor cells delivered in a melittin hydrogel potentiate cancer immunotherapy, Bioact. Mater. 9 (2022) 541–553.
[29] D. Kim, Y. Wu, G. Shim, Y.K. Oh, Genome-editing-mediated restructuring of tumor immune microenvironment for prevention of metastasis, ACS Nano 15 (11) (2021) 17635–17656.
[30] T. Chanmee, P. Ontong, K. Konno, N. Itano, Tumor-associated macrophages as major players in the tumor microenvironment, Cancers 6 (3) (2014) 1670–1690.
[31] A. Angelin, L. Gil-de-Gómez, S. Dahiya, J. Jiao, L. Guo, M.H. Levine, Z. Wang, W. J. Quinn, P.K. Kopinski, L. Wang, Foxp3 reprograms T cell metabolism to function in low-glucose, high-lactate environments, Cell Metabol. 25 (6) (2017) 1282–1293.
[32] L. Zhang, Y. Jia, J. Yang, L. Zhang, S. Hou, X. Niu, J. Zhu, Y. Huang, X. Sun, Z. P. Xu, R. Liu, Efficient immunotherapy of drug-free layered double hydroxide nanoparticles via neutralizing excess acid and blocking tumor cell autophagy, ACS Nano 16 (8) (2022) 12036–12048.
[33] J. Xie, L. Gong, S. Zhu, Y. Yong, Z. Gu, Y. Zhao, Emerging strategies of nanomaterial-mediated tumor radiosensitization, Adv. Mater. 31 (3) (2019), 1802244.
[34] Z. Shi, R. Cao, K. Khan, A.K. Tareen, X. Liu, W. Liang, Y. Zhang, C. Ma, Z. Guo, X. Luo, H. Zhang, Two-dimensional tellurium: progress, challenges, and prospects, Nano-Micro Lett. 12 (1) (2020) 99.
[35] Y. Dai, T. Li, Z. Zhang, Y. Tan, S. Pan, L. Zhang, H. Xu, Oxidative polymerization in living cells, J. Am. Chem. Soc. 143 (28) (2021) 10709–10717.
[36] M. Chen, W. Cao, J. Wang, F. Cai, L. Zhu, L. Ma, T. Chen, Selenium atom-polarization effect determines TrxR-specific recognition of metallodrugs, J. Am. Chem. Soc. 144 (45) (2022) 20825–20833.
[37] Y. Wu, T. Guo, Y. Qiu, Y. Lin, Y. Yao, W. Lian, L. Lin, J. Song, H. Yang, An inorganic prodrug, tellurium nanowires with enhanced ROS generation and GSH depletion for selective cancer therapy, Chem. Sci. 10 (29) (2019) 7068–7075.
[38] T. Yang, H. Ke, Q. Wang, Y. Tang, Y. Deng, H. Yang, X. Yang, P. Yang, D. Ling, C. Chen, Y. Zhao, H. Wu, H. Chen, Bifunctional tellurium nanodots for photo-induced synergistic cancer therapy, ACS Nano 11 (10) (2017) 10012–10024.
[39] W. Huang, H. Wu, X. Li, T. Chen, Facile one-pot synthesis of tellurium nanorods as antioxidant and anticancer agents, Chem. Asian J. 11 (16) (2016) 2301–2311.
[40] F. Zhao, W. Huang, L. He, S. Nie, Z. Sun, T. Chen, H. Yin, J. Zhao, Reversing lung cancer radioresistance by hyperpermeable tellurium nanotherapeutics via remodeling tumor microenvironment, Nano Today 50 (2023), 101819.
[41] H. Zhang, X. Pan, Q. Wu, J. Guo, C. Wang, H. Liu, Manganese carbonate nanoparticles-mediated mitochondrial dysfunction for enhanced sonodynamic therapy, Explorations 1 (2) (2021) 1–12.
[42] Y. Cheng, S. Zhang, N. Kang, J. Huang, X. Lv, K. Wen, S. Ye, Z. Chen, X. Zhou, L. Ren, Polydopamine-coated manganese carbonate nanoparticles for amplified magnetic resonance imaging-guided photothermal therapy, ACS Appl. Mater. Interfaces 9 (22) (2017) 19296–19306.
[43] P. Wang, C. Liang, J. Zhu, N. Yang, A. Jiao, W. Wang, X. Song, X. Dong, Manganese-based nanoplatform as metal ion-enhanced ROS generator for combined chemodynamic/photodynamic therapy, ACS Appl. Mater. Interfaces 11 (44) (2019) 41140–41147.
[44] P. Bao, Z.T. Zheng, J.J. Ye, X.Z. Zhang, Apoptotic body-mediated intracellular delivery strategy for enhanced STING activation and improved tumor immunogenicity, Nano Lett. 22 (6) (2022) 2217–2227.
[45] C. Wang, Y. Guan, M. Lv, R. Zhang, Z. Guo, X. Wei, X. Du, J. Yang, T. Li, Y. Wan, X. Su, X. Huang, Z. Jiang, Manganese increases the sensitivity of the cGAS-STING pathway for double-stranded DNA and is required for the host defense against DNA viruses, Immunity 48 (4) (2018) 675–687 e677.
[46] L. Tian, X. Yi, Z. Dong, J. Xu, C. Liang, Y. Chao, Y. Wang, K. Yang, Z. Liu, Calcium bisphosphonate nanoparticles with chelator-free radiolabeling to deplete tumor-associated macrophages for enhanced cancer radioisotope therapy, ACS Nano 12 (11) (2018) 11541–11551.
[47] Tumor microenvironment-activatable Fe-doxorubicin preloaded amorphous CaCO3 nanoformulation triggers ferroptosis in target tumor cells, Sci. Adv. 6 (2020) eaax1346.
[48] Q. Chen, C. Wang, X. Zhang, G. Chen, Q. Hu, H. Li, J. Wang, D. Wen, Y. Zhang, Y. Lu, G. Yang, C. Jiang, J. Wang, G. Dotti, Z. Gu, In situ sprayed bioresponsive immunotherapeutic gel for post-surgical cancer treatment, Nat. Nanotechnol. 14 (1) (2019) 89–97.
[49] D. Cen, Q. Ge, C. Xie, Q. Zheng, J. Guo, Y. Zhang, Y. Wang, X. Li, Z. Gu, X. Cai, ZnS@BSA nanoclusters potentiate efficacy of cancer immunotherapy, Adv. Mater. 33 (49) (2021), 2104037.
[50] S. Pan, G. Huang, Z. Sun, X. Chen, X. Xiang, W. Jiang, Y. Xu, T. Chen, X. Zhu, X-Ray-Responsive zeolitic imidazolate framework-capped nanotherapeutics for cervical cancer-targeting radiosensitization, Adv. Funct. Mater. (2023), 2213364.
[51] J. Xiao, G. Zhang, R. Xu, H. Chen, H. Wang, G. Tian, B. Wang, C. Yang, G. Bai, Z. Zhang, H. Yang, K. Zhong, D. Zou, Z. Wu, A pH-responsive platform combining chemodynamic therapy with limotherapy for simultaneous bioimaging and synergistic cancer therapy, Biomaterials 216 (2019), 119254.
[52] Z. Yuan, X. Liu, J. Ling, G. Huang, J. Huang, X. Zhu, L. He, T. Chen, In situ-transition nanozyme triggered by tumor microenvironment boosts synergistic cancer radio-/chemotherapy through disrupting redox homeostasis, Biomaterials 287 (2022), 121620.
[53] B. Zou, Z. Xiong, L. He, T. Chen, Reversing breast cancer bone metastasis by metal organic framework-capped nanotherapeutics via suppressing osteoclastogenesis, Biomaterials 285 (2022), 121549.
[54] C. Qi, J. He, L.H. Fu, T. He, N.T. Blum, X. Yao, J. Lin, P. Huang, Tumor-specific activatable nanocarriers with gas-generation and signal amplification capabilities for tumor theranostics, ACS Nano 15 (1) (2021) 1627–1639.
[55] L.A. Ba, M. Doring, V. Jamier, C. Jacob, Tellurium: an element with great biological potency and potential, Org. Biomol. Chem. 8 (19) (2010) 4203–4216.
[56] W. Li, Y. Wang, D. Xue, L. Jin, Y. Liu, Z. Lv, Y. Cao, R. Niu, H. Zhang, S. Zhang, B. Xu, N. Yin, S. Zhang, H. Zhang, A novel biodegradable nanoplatform for tumor microenvironments responsive bimodal magnetic resonance imaging and sonodynamic/ion interference cascade therapy, ACS Appl. Mater. Interfaces 14 (45) (2022) 50616–50625.
[57] K.H. Min, H.S. Min, H.J. Lee, D.J. Park, J.Y. Yhee, K. Kim, I.C. Kwon, S.Y. Jeong, O. F. Silvestre, X. Chen, Y.S. Hwang, E.C. Kim, S.C. Lee, pH-controlled gas-generating mineralized nanoparticles: a theranostic agent for ultrasound imaging and therapy of cancers, ACS Nano 9 (1) (2015) 134–145.
[58] X. Dong, R. Cheng, S. Zhu, H. Liu, R. Zhou, C. Zhang, K. Chen, L. Mei, C. Wang, C. Su, A heterojunction structured WO2. 9-WSe2 nanoradiosensitizer increases local tumor ablation and checkpoint blockade immunotherapy upon low radiation dose, ACS Nano 14 (5) (2020) 5400–5416.
[59] Xue Yang, Ying Yang, Jiayi Bian, Jiajia Wei, Zheng Wang, Zhanwei Zhou, Zhaoting Li, M. Sun, Converting primary tumor towards an in situ STING activating vaccine via a biomimetic nanoplatform against recurrent and metastatic tumors, Nano Today (2021), 101109.
[60] L. Hou, C. Tian, Y. Yan, L. Zhang, H. Zhang, Z. Zhang, Manganese-based nanoactivator optimizes cancer immunotherapy via enhancing innate immunity, ACS Nano 14 (4) (2020) 3927–3940.
[61] H. Phuengkham, L. Ren, I.W. Shin, Y.T. Lim, Nanoengineered immune niches for reprogramming the immunosuppressive tumor microenvironment and enhancing cancer immunotherapy, Adv. Mater. 31 (34) (2019), 1803322.
[62] C. Song, H. Phuengkham, Y.S. Kim, V.V. Dinh, I. Lee, I.W. Shin, H.S. Shin, S.M. Jin, S.H. Um, H. Lee, Syringeable immunotherapeutic nanogel reshapes tumor microenvironment and prevents tumor metastasis and recurrence, Nat. Commun. 10 (1) (2019) 3745.
[63] B. Medeiros, A.L. Allan, Molecular mechanisms of breast cancer metastasis to the lung: clinical and experimental perspectives, Int. J. Mol. Sci. 20 (9) (2019) 2272.
[64] Y. Xiao, M. Cong, J. Li, D. He, Q. Wu, P. Tian, Y. Wang, S. Yang, C. Liang, Y. Liang, Cathepsin C promotes breast cancer lung metastasis by modulating neutrophil infiltration and neutrophil extracellular trap formation, Cancer Cell 39 (3) (2021) 423–437.
[65] L. He, T. Nie, X. Xia, T. Liu, Y. Huang, X. Wang, T. Chen, Designing bioinspired 2D MoSe2 nanosheet for efficient photothermal-triggered cancer immunotherapy with reprogramming tumor-associated macrophages, Adv. Funct. Mater. 29 (30) (2019), 1901240.
[66] G. Yang, L. Xu, Y. Chao, J. Xu, X. Sun, Y. Wu, R. Peng, Z. Liu, Hollow MnO(2) as a tumor-microenvironment-responsive biodegradable nano-platform for combination therapy favoring antitumor immune responses, Nat. Commun. 8 (1) (2017) 902.
[67] C. Liang, L. Xu, G. Song, Z. Liu, Emerging nanomedicine approaches fighting tumor metastasis: animal models, metastasis-targeted drug delivery, phototherapy, and immunotherapy, Chem. Soc. Rev. 45 (22) (2016) 6250–6269.